THE GEOLOGICAL SOCIETY
OF AMERICA®

Early to middle Eocene (50–43 Ma) Xianqian Basin in central Tibet: Archives of arid paleoenvironments and a southward plateau uplift trend

Anlin Ma[1,†], John J.Y. He[2], Xiumian Hu[1,†], Paul Kapp[3], Youwei Wang[4], Jordan W. Wang[2], Lin Li[5], Wendong Liang[6], Xuetian Wang[7], and Keran Li[1]

[1]*State Key Laboratory of Critical Earth Material Cycling and Mineral Deposits, School of Earth Sciences and Engineering, Nanjing University, Nanjing 210023, China*
[2]*Department of Earth, Planetary, and Space Sciences, University of California, Los Angeles, California 90095-1567, USA*
[3]*Department of Geosciences, University of Arizona, Tucson, Arizona 85721, USA*
[4]*Department of Environmental Sciences, University of Virginia, Charlottesville, Virginia 22904, USA*
[5]*Department of Earth, Environmental and Geographical Sciences, University of North Carolina–Charlotte, Charlotte, North Carolina 28223, USA*
[6]*State Key Laboratory of Oil and Gas Reservoir Geology and Exploitation, Institute of Sedimentary Geology, Chengdu University of Technology, Chengdu 610059, China*
[7]*College of Geoscience and Surveying Engineering, China University of Mining and Technology (Beijing), Beijing 100083, China*

ABSTRACT

Sedimentary basins provide valuable records of local surface uplift and paleoenvironment. While previous studies have inferred that the Qiangtang terrane in the Tibetan interior has been at high elevation since at least the Eocene, direct evidence from well-dated basins within the Qiangtang terrane remains scarce. Here, we present integrated stratigraphic, sedimentologic, paleontologic, and provenance data from the Maerguo Formation in the Xianqian Basin, southwestern Qiangtang. U-Pb dating of tuff zircons and lacustrine carbonate indicates that the Maerguo Formation was deposited between ca. 50 Ma and 43 Ma, establishing an Eocene record for central Tibet's paleoenvironmental, tectonic, and topographic evolution. The Maerguo Formation consists of >1900 m of well-exposed strata that comprise five distinct units from bottom to top: Em_1 (lower conglomerates); Em_2 (fluvial red beds); Em_3 (lower fine-grained lacustrine red beds); Em_4 (upper lacustrine unit); and Em_5 (upper conglomerates). Growth strata developed synchronously with a north-dipping thrust along the northern margin of the Xianqian Basin, while the southern part of the basin dips gently and lies unconformably above Mesozoic strata. Multiproxy provenance data indicate sediment sources from surrounding sedimentary and volcanic rocks, with sediments derived from more localized metamorphic rocks and Jurassic granitoids to the north becoming dominant during the deposition of units Em_4 and Em_5 in the northern basin. The presence of abundant gypsum in Em_3, lacustrine carbonate in Em_3 and Em_4, and small, narrow, elongate leaf fossils in Em_4 indicates an arid environment. These findings indicate that the Xianqian Basin was a short-lived, arid, internally drained system that terminated well before the peak expansion of Cenozoic basins along the Bangong-Nujiang suture to the south. The integrated paleogeographic reconstruction suggests that surface uplift of the Tibetan Plateau progressed southward from its interior since the Eocene. This Tibetan uplift pattern may have been driven by lithospheric removal and associated crustal shortening and thickening, beginning in the central Qiangtang terrane.

1. INTRODUCTION

The Tibetan Plateau, the largest and highest plateau on Earth, has experienced a complex uplift history since the Mesozoic due to the successive suturing of multiple terranes (Dewey et al., 1988; Yin and Harrison, 2000; Wang et al., 2008a; Kapp and DeCelles, 2019; Spicer et al., 2021; Ding et al., 2022). Evidence indicates the presence of an Andean-type Gangdese magmatic arc >3 km in paleoelevation just before the India-Asia collision in the southern Lhasa terrane of southern Tibet (Ibarra et al., 2023), and this high topography persisted into the early Cenozoic (Ding et al., 2014; Ingalls et al., 2018).

Farther to the north, the Bangong-Nujiang suture zone in central Tibet divides the Lhasa and Qiangtang terranes and hosts several Cenozoic nonmarine basins that record signals of early Cenozoic low elevation (Xu et al., 1985; Rowley and Currie, 2006; DeCelles et al., 2007; Wang et al., 2011; Wei et al., 2016; Han et al., 2019). Among these basins, the Lunpola-Bangoin-Nima basin in the east is well constrained to have been wet and at a low elevation during the Paleocene to Eocene (Wu et al., 2017; Su et al., 2019, 2020; Fang et al., 2020; Xiong et al., 2022; Li et al., 2022b, 2024b). The Gerze basin to the west was suggested to be near sea-level elevation during the Eocene (Wei et al., 2016), though supporting evidence has been argued to be insufficient (Li et al., 2024a).

By contrast, paleoelevation estimates are less well constrained for the Qiangtang terrane. Though low $\delta^{18}O$ values from strata of poorly constrained depositional age (e.g., some time between ca. 51 Ma and 28 Ma) suggest >5000 m (Xu et al., 2013) or >2830 m of paleoelevation (Shen et al., 2023), oxygen isotope records in Tibet are prone to diagenetic alteration and thus require careful assessment (Quade et al., 2020; Li et al., 2024a, 2024c). Other evidence indirectly suggests that the Qiangtang terrane may have been uplifted as an orogenic plateau during the Eocene, including (1) weakly deformed flat-lying Eocene to Oligocene volcanic rocks (Law

---

Anlin Ma https://orcid.org/0000-0001-6893-6583
†Anlin Ma, alma@nju.edu.cn; Xiumian Hu, huxm@nju.edu.cn

GSA Bulletin;
Published online 13 November 2025

https://doi.org/10.1130/B38437.1.

and Allen, 2020) and (2) regional exhumation of rocks to <3 km crustal depth by ca. 45 Ma (Rohrmann et al., 2012). However, these lines of evidence alone do not necessitate the existence of a high-elevation plateau.

Cenozoic sedimentary basins in the Qiangtang terrane provide an opportunity to better reconstruct its paleoenvironment and paleotopographic history. Previous studies have grouped Cenozoic strata across the Qiangtang terrane into the lower coarse-grained Kangtuo Formation and the upper fine-grained Suonahu Formation, interpreted to have been deposited in alluvial fans and lacustrine environments, respectively (Xia and Liu, 1997). However, only a few Paleogene radioisotopic ages are available for these strata (Xu et al., 2013; Wang et al., 2019; Zhang et al., 2024), and systematic studies of these units at the scale of individual basins are still lacking.

In this paper, we report the results of an investigation of the Maerguo Formation from the Eocene Xianqian Basin in the southwestern Qiangtang terrane (Fig. 1). Our detailed measured stratigraphic sections of the Maerguo Formation show that it consists of an ~2-km-thick package of coarse- to fine-grained clastic, carbonate, gypsum, and volcaniclastic strata. A major portion (472 m) of the upper Maerguo Formation consists of deep-water lacustrine gravity-flow deposits. Geologic mapping, multiproxy sediment provenance data, and fossils further illuminate the paleoenvironmen-

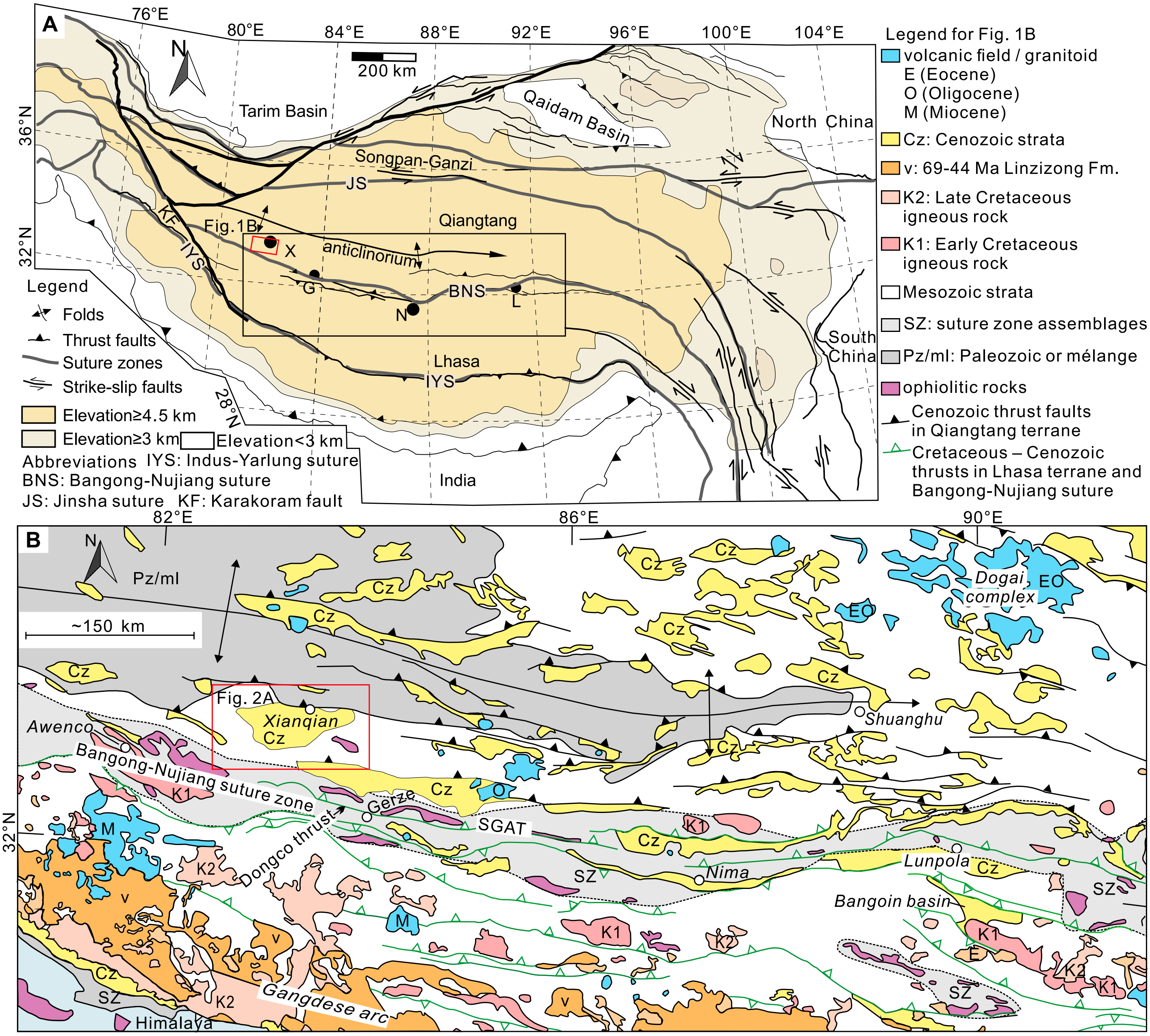

Figure 1. Regional geological map showing the location of the Xianqian Basin. (A) Tectonic framework of the Tibetan Plateau (after DeCelles et al., 2011). The Xianqian Basin (X) is located in central western Tibet. G—Gertze; N—Nima; L—Lunpola. (B) Geologic map of central-southern Tibet after Kapp and DeCelles (2019). SGAT—Shiquanhe-Gerze-Amdo thrust system.

tal, paleogeographic, and tectonic evolution of the Xianqian Basin. The data we present here indicate that the 50–43 Ma Maerguo Formation was deposited in the footwall of a coeval north-dipping thrust fault and was located in a region much drier and likely higher in elevation than previously documented contemporaneous basins within the Bangong-Nujiang suture zone to the south (Gerze, Nima, and Lunpola Basins). The stratigraphic architecture, syncontractional setting, abundance of tuffs and tuffaceous breccias in the upper part of the Maerguo Formation, and the relatively short-lived nature of the Xianqian Basin are broadly consistent with a basin-forming mechanism influenced by integrated upper-crustal shortening and magmatism related to removal of lower lithosphere.

2. GEOLOGIC BACKGROUND

The Qiangtang terrane, bounded by the Jinsha suture to the north and the Bangong-Nujiang suture to the south, constitutes the middle of the physiographic Tibetan Plateau (Fig. 1A). The terrane-scale eastward-plunging Qiangtang anticlinorium exposes early Paleozoic pan-African granitoid basement, Triassic high-pressure–high-temperature metamorphic rocks, and Paleozoic passive-margin strata in its core (Pullen and Kapp, 2014; Xu et al., 2020). Jurassic shallow-marine strata are widespread along the limbs of the anticlinorium (Ma et al., 2023a). During Jurassic–Early Cretaceous time, the Bangong-Nujiang (Meso-Tethys) oceanic plate subducted northward beneath the Qiangtang terrane, resulting in continental arc magmatism with peak ages of 170–150 Ma and 110 Ma and an intervening magmatic lull at 140–130 Ma (Zhu et al., 2016). The Qiangtang terrane was uplifted above sea level during the latest Jurassic to Early Cretaceous due to Lhasa-Qiangtang suturing (Ma et al., 2017, 2018; Hu et al., 2022; Ma et al., 2023a). The nonmarine red beds of the Abushan Formation were deposited in intermontane basins during mid- to Late Cretaceous time, along with coeval (100–70 Ma) high-K volcanic rocks (Li et al., 2013b; He et al., 2018; Ma et al., 2023b; Wen et al., 2023), indicating that the Qiangtang terrane had become a significant orogenic belt prior to the Cenozoic India-Asia collision. Cenozoic red beds in the Qiangtang terrane have generally been assigned to the Kangtuo and Suonahu Formations without systematic geochronologic constraints (Mou et al., 2005; Yue et al., 2006). Distinguishing these formations from each other and from the Abushan Formation is challenging because of the lack of robust age control and similarity in lithology among these formations. In addition, the Qiangtang terrane exposes weakly deformed to undeformed Eocene to Oligocene alkaline and adakitic volcanic rocks within scattered elliptical areas, among which the Dogai complex is the largest (Fig. 1B; Wang et al., 2008b; Kapp and DeCelles, 2019; Zeng et al., 2021; McMillan and Schoenbohm, 2023).

The Xianqian Basin is oval-shaped and located in the southwest part of the Qiangtang terrane (Figs. 1B and 2A). Most red beds within the Xianqian Basin were previously mapped as the Cretaceous Abushan Formation (1:250,000 geologic map of the Jiacuo area by the Chinese Geological Survey; He et al., 2006). However, in this study, we demonstrated their Eocene depositional age through U-Pb zircon dating of interbedded tuffs and stratigraphic correlation. We thus define the Maerguo Formation as a distinct stratigraphic unit in the Xianqian Basin. The Maerguo Formation unconformably overlies or is structurally bounded by Lower Cretaceous felsic volcanic rocks, 165–160 Ma granitoid rocks, Paleozoic and Jurassic limestone and clastic rocks, and Cretaceous nonmarine red beds in different locations along the basin margins (Fig. 2A).

Several other Cenozoic nonmarine basins are scattered along the Bangong-Nujiang suture zone, ∼30 km to the south of the Xianqian Basin, including the Lunpola-Nima, Gerze, and Awenco basins from east to west (Fig. 1B). The Bangong-Nujiang suture includes mainly Jurassic deep-marine turbidite-bearing strata and ophiolites that represent the relics of the subducted Bangong-Nujiang (Meso-Tethys) Ocean (Hu et al., 2022). This suture was uplifted above sea level during the Late Jurassic–Early Cretaceous collision between the Lhasa and Qiangtang terranes, which was diachronous along strike (decreasing in age from east to west; Kapp et al., 2007; DeCelles, et al., 2007; Ma et al., 2018, 2024). The Cenozoic basins postdate closure of the Meso-Tethys Ocean and provide important geologic records for postcollisional paleoenvironment and paleoaltimetry. We explore the development of these basins in relation to the Xianqian Basin later in the paper to better understand the regional development of topography and paleoenvironmental changes in central Tibet.

3. METHODS

3.1. Field Geology

Stratigraphic sections were measured using a tape measure at the decimeter scale. Lithofacies codes adapted from Miall (1977) and DeCelles et al. (2007) were used for logging and interpreting sedimentary features (Table 1). Paleocurrent data were measured from dune-scale trough and planar cross-stratification (DeCelles et al., 1983). Samples for geochronology, sedimentary petrology, and paleontology were collected in the context of the measured sections. For conglomerates, the lithologies of ∼100 clasts were determined within a 1 m^2 area in each outcrop site for provenance interpretation; the results are provided in Table S1 in the Supplemental Material.[1]

3.2. Framework Composition and Heavy-Mineral Suite of Sandstone

In total, 73 sandstone samples from the Maerguo Formation were prepared as 30-μm-thick thin sections for petrographic analysis. The modal framework-grain composition was determined by point counting ≥400 grains per slide under a polarized microscope, following the Gazzi-Dickinson method (Gazzi, 1966; Ingersoll et al., 1984). Grain types and results are provided in Table S2.

Fifteen samples from the Maerguo Formation were selected for heavy-mineral analysis. Sandstone samples were hand-crushed using an agate mortar, and the 32–500 μm size fraction was obtained by wet sieving. Heavy minerals were separated by centrifugation in sodium polytungstate (density: 2.90 g/cm^3) and recovered through partial freezing with liquid nitrogen. The dense fraction was then mounted on a slide using Canada balsam, and ≥200 transparent heavy minerals (or all present in the grain mount) were point-counted at regular intervals to determine accurate volume percentages (Garzanti and Andò, 2019). Transparent heavy-mineral assemblages were defined as the spectrum of detrital allochthonous minerals with a density >2.90 g/cm^3, identifiable under a transmitted light microscope. The sum of zircon, tourmaline, and rutile relative to the total transparent heavy minerals (ZTR index of Hubert, 1962) quantifies the relative proportion of durable minerals within the assemblage and serves as an indicator of sediment recycling (Garzanti, 2017). These results are provided in Table S3.

3.3. Zircon U-Pb Dating

Zircons were extracted from seven sandstone (23NR84, 23NR18, 23GZ46, 23NR54, 23NR60, 23TG01, and 23TG14), four magmatic rock (23GZ41, 23NR83, 23NR50, and 23XQ271), and one tuff (23XQ316) samples through crush-

---

[1] Supplemental Material. Figures and dataset supporting this study. Please visit https://doi.org/10.1130/GSAB.S.30359200 to access the supplemental material; contact editing@geosociety.org with any questions.

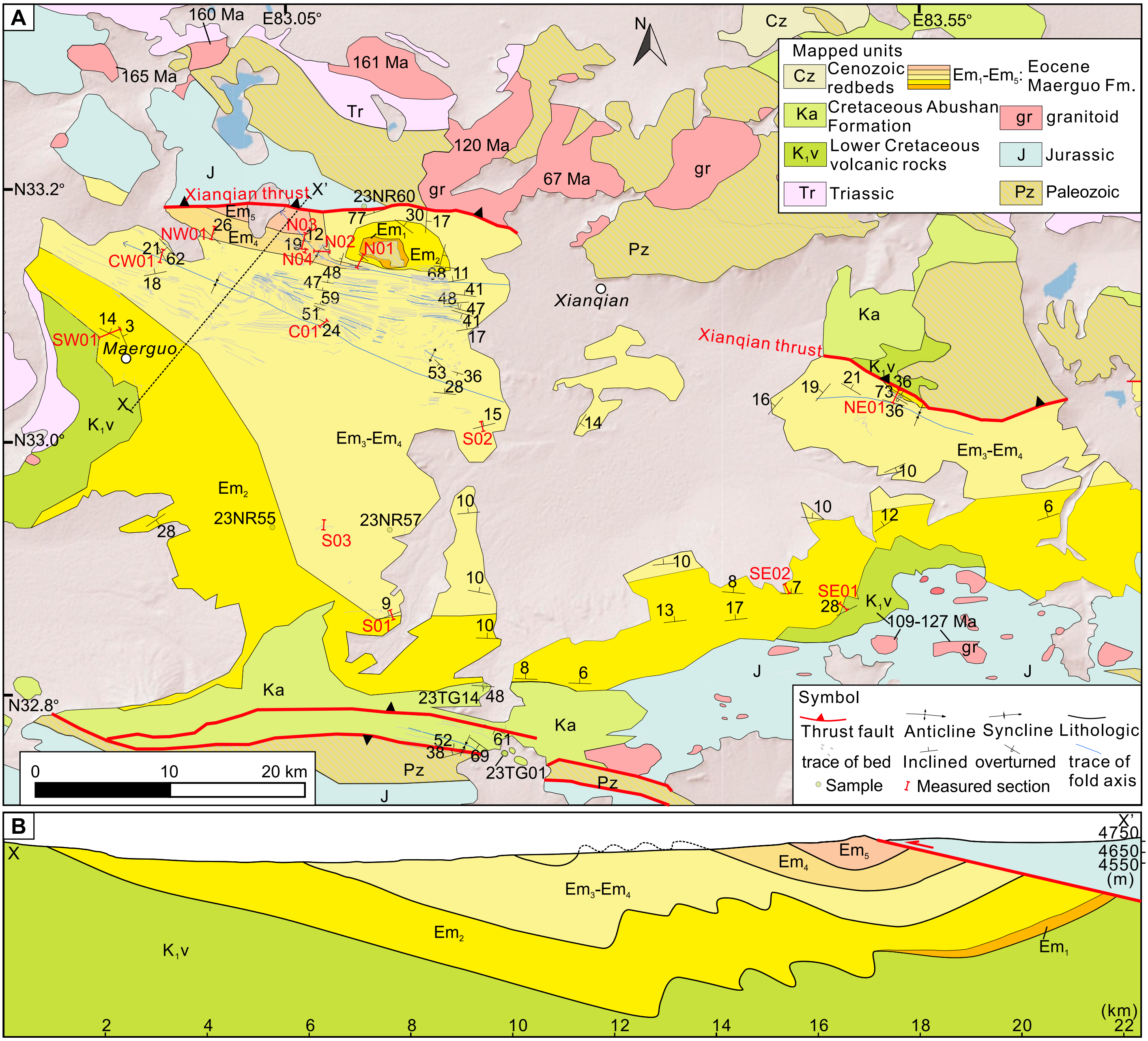

Figure 2. (A) Geologic map and (B) schematic geologic cross section of the Xianqian Basin. Geologic map was modified after the map produced by the Chinese Geological Survey (Mou et al., 2005) by integrating our own mapping data. Ages of igneous rocks are from the Tibetan Magmatism Database (Chapman and Kapp, 2017).

ing, elutriation, and magnetic separation. For detrital zircons from sandstone, ~120 grains were dated per sample; for magmatic rock and tuff, ~20 grains were analyzed per sample.

Zircon grains from the sandstone and magmatic rocks were randomly picked and mounted in epoxy and polished to expose grain interiors. Zircon U, Th, and Pb isotopes were measured at the State Key Laboratory of Critical Earth Material Cycling and Mineral Deposits, Nanjing University, utilizing an ASI RESOlution S-155 193 nm ArF excimer laser coupled with a Thermo Scientific iCAP Qc quadrupole inductively coupled plasma–mass spectrometer (ICP-MS). U-Pb age data were collected by laser ablation with a beam diameter of 30 μm, a beam energy density of ~3.5 J/cm^2, and a repetition rate of 5 Hz. Each analysis included 20 s of background, 50 s of ablation, and 20 s of washout. With an ablation rate of ~0.1 μm/pulse, 50 s of ablation with a 30 μm beam diameter produces an ablation crater with a diameter/depth ratio of <1. The ^{207}Pb/^{206}Pb, ^{206}Pb/^{238}U, ^{207}Pb/^{235}U (^{235}U = ^{238}U/137.88), and ^{208}Pb/^{232}Th ratios were corrected using the zircon standard 91500 as an external standard (isotope dilution–thermal ionization mass spectrometry ^{206}Pb/^{238}U age date at 1062.4 ± 0.8 Ma; Wiedenbeck et al., 1995). Plešovice and GEMOC GJ-1 standards were applied as quality-control references. Zircon standards were analyzed every 15 unknown samples. Data reduction was performed with ICPMSDataCal software (Liu et al., 2010). The

TABLE 1. LITHOFACIES FOR SEDIMENTARY ROCKS OF THE MAERGUO FORMATION IN THE XIANQIAN BASIN, WITH INTERPRETATIONS OF THEIR DEPOSITIONAL PROCESSES

Lithofacies code	Description	Interpretation
Gcm	Clast-supported, pebble-cobble, poorly sorted, unstratified	Deposition from clast-rich debris flows and sheetfloods
Gch, Gchi	Clast-supported, pebble-cobble, medium to well sorted, horizontally stratified, imbricated (long-axis transverse to paleoflow)	Shallow traction currents in longitudinal bars, or sieve deposits in alluvial fans
Gt	Clast-supported, pebble to boulder, trough cross-stratified conglomerate	Deposition by large gravelly ripples under traction flows in relatively deep, stable fluvial channels
Sm	Massive medium- to coarse-grained sandstone, sometimes pebbly and lens-like	High rate of deposition, highly concentrated, sand-rich deposits, probably formed during high-discharge periods
Sh	Medium- to very coarse-grained sandstone, horizontally stratified, sometimes pebbly	Plane-bed flow under strong or very shallow unidirectional flow
St	Fine- to coarse-grained sandstone, trough stratified	Sinuously crested and linguoid (3-D) dunes under moderately powerful, unidirectional flow in large channels
Sp	Medium- to very coarse-grained sandstone with planar cross-stratification	Migration of large two-dimensional (2-D) ripples under moderately powerful, unidirectional channelized flows or migration of sandy transverse bars
Sr	Fine- to medium-grained sandstone, with asymmetric two- and three-dimensional (3D) current ripples	Migration of small 2-D and 3-D ripples under weak unidirectional flows in shallow channels
Sb	Bioturbated sandstone	Trace fossils formed by insects, dwelling, resting, crawling
F	Siltstone and mudrock	Suspension setting in overbank, abandoned channel, waning flood deposits, or subaqueous lake
M	Marlstone/micritic carbonate	Lacustrine carbonate mud with insignificant siliciclastic influx
Gyp	Gypsum	Lacustrine evaporite in an arid environment
Vb	Tuffaceous breccia, thick- to medium-bedded, gray, including breccia of pebbles and granule size and dominated by mudrock	Pyroclastic flow into the lake
Vt	Volcanic glass–dominated tuff, mostly thin to medium bedded, with massive-bedded locally, and gray or green in color	Suspension fallout, or transported though river punching into the lake

Note: Modified after Miall (1977) and DeCelles et al. (2007).

measured Plešovice and GJ-1 yielded weighted mean ^{206}Pb/^{238}U ages of 337.2 ± 2.0 Ma ($n = 23$, mean square of weighted deviates [MSWD] = 0.09) and 599.8 ± 2.0 Ma ($n = 55$, MSWD = 0.038), respectively (Fig. S2), in agreement with the recommended ^{206}Pb/^{238}U ages of Plešovice (^{206}Pb/^{238}U age = 337 Ma; Sláma et al., 2008) and GJ-1 (^{206}Pb/^{238}U age = 602.7–598.5 Ma; Jackson et al., 2004). The ^{206}Pb/^{238}U zircon age was used for interpretation where the ^{206}Pb/^{238}U age was younger than 1000 Ma, and the ^{207}Pb/^{206}Pb age was used if the ^{206}Pb/^{238}U age was older than 1000 Ma. Ages older than 400 Ma with >30% (^{207}Pb/^{235}U vs. ^{206}Pb/^{207}Pb) discordance were removed from consideration, while grains younger than 400 Ma with >10% discordance (^{207}Pb/^{235}U vs. ^{206}Pb/^{238}U) were also excluded. The results are provided in Table S4.

Zircons from tuff sample 23XQ316 and standards (Plešovice and Qinghu) were comounted in a single epoxy target and polished to expose grain interiors. Secondary ion mass spectrometry (SIMS) U-Pb dating was conducted using a Cameca IMS-1300HR[3] at the State Key Laboratory of Critical Earth Material Cycling and Mineral Deposits, Nanjing University. Reflected and transmitted light microscopy and cathodoluminescence (CL) imagery were used to aid the selection of analysis spots. A 3 nA primary O^- ion beam spot ~15 × 10 μm in size was applied to impact on the gold-coated surface of zircon grains. Positive secondary ions were extracted with a 10 kV potential. In the secondary ion beam optics, a 60 eV energy window was used, together with a mass resolution of ~7000 ($M/\Delta M$; at 50% peak height), to separate Pb^+ peaks from isobaric interferences. A single electron multiplier was used in ion-counting mode to measure secondary ion beam intensities by peak-jumping mode. Each measurement consisted of eight cycles. Analyses of the standard zircon Plešovice were interspersed with unknown grains. Pb/U calibration was performed relative to the zircon standard Plešovice (^{206}Pb/^{238}U age = 337 Ma; Sláma et al., 2008). Measured compositions were corrected for common Pb using nonradiogenic ^{204}Pb. Corrections were sufficiently small to be insensitive to the choice of common Pb composition, and an average of present-day crustal composition (Stacey and Kramers, 1975) was used for the common Pb, assuming that the common Pb was largely surface contamination introduced during sample preparation. In order to monitor the external uncertainties of SIMS U-Pb zircon dating calibrated against the Plešovice standard (Sláma et al., 2008), an in-house zircon standard Qinghu (Li et al., 2013a) was alternately analyzed as an unknown. The isotopic and age dataset obtained by SIMS is detailed in Table S5. The U-Pb concordia diagrams and corresponding weighted mean ^{206}Pb/^{238}U age plots for the zircon standards are shown in Figure S2.

3.4. Carbonate U-Pb Dating

Carbonate U-Pb dating of one limestone sample (23NR93) was carried out using a Thermo Fisher Neptune Plus multicollector (MC) ICP-MS in combination with a RESOlution S155LR 193 nm ArF excimer laser-ablation system at the Mineral Laser Microprobe Analysis Laboratory (Milma Lab), China University of Geosciences, Beijing (CUGB). The detailed instrumental and experimental parameters were described in Zhang et al. (2021). Data were acquired on thin sections. Due to the widespread element and isotope heterogeneity of carbonate minerals, the grid diagram method was used to divide the sample into many regions, and then each region was ablated sequentially under optimized instruments parameters with ^{238}U signal intensity of 8–12 mV and ^{207}Pb/^{206}Pb of Standard Reference Material (SRM) NIST-614 of ~1 (Zhang et al., 2021). Finally, the areas with relatively high U (^{238}U signal intensity >2.5 mV) and low common Pb content (variable or low ^{207}Pb/^{206}Pb ratios) were selected as the formal ablation areas. A laser spot size of 90 μm, a laser energy density of 2 J/cm^2, and a repetition rate of 10 Hz were employed during the analysis. Helium was used as carrier gas, while argon and nitrogen were used as makeup and enhancement gases. Each analysis was composed of 20 s background time followed by 30 s of ablation and then 30 s of washout. Unknown samples were corrected by standard bracketing with synthetic SRM NIST-614 glass for instrumental drift and Pb isotope composition (Woodhead and Hergt, 2000) and a natural calcite WC-1 of 254.4 ± 6.4 Ma (Roberts et al., 2017) to correct for ^{206}Pb/^{238}U fractionation. Calcite reference material Tarim with an age of 208.0 ± 0.4/3.2 Ma (Zhang et al., 2023) was measured to provide a control on accuracy and precision. These measurements yielded Tera-Wasserburg concordia intercept ages of 207.8 ± 1.4 Ma ($n = 22$, MSWD = 0.38), which is consistent with the published ages within the analytical uncertainty. Raw data reduction was performed off-line using Iolite v3.73 software (Paton et al., 2011). The Isoplot 4.15 software (Ludwig, 2008) was used to calculate the U-Pb ages and generate the Tera-Wasserburg diagrams. Age errors are presented at the 95% confidence level, and error ellipses are given as 2σ. The data results and Tera-Wasserburg diagrams of calcite reference material Tarim are provided in Table S6.

3.5. Tectonic Subsidence Analysis

The tectonic subsidence analysis was based on the high-precision age-depth data from the Xianqian Basin, following the backstripping method outlined by Allen and Allen (2005) to remove the effects of sediment loads and water-depth variations. Decompaction of stratigraphic units was applied to eliminate the effect of the exponential decrease of porosity with depth during progressive burial, before an Airy isostatic model was adopted to subtract sediment load, with the sediment lithologies and densities determined based on our measured section and comparable lithologies listed in Allen and Allen (2005). Paleowater depth deepened from 0 m in the alluvial and fluvial units Em_1 and Em_2 to >5–15 m in the lacustrine unit Em_4, which contains gravity-flow deposits, based on our sedimentologic observations and interpretations (see next section).

4. RESULTS

4.1. Stratigraphy and Sedimentology

The Eocene Maerguo Formation consists of an ~930 m fining-upward subsequence and then an ~967 m coarsening-upward subsequence, which combined reach nearly 2 km in thickness (Fig. 3). Preliminary mapping showed that the Maerguo Formation is strongly deformed, with tight folds in the central Xianqian Basin that broaden to the north and south (Fig. 2B). In the northern Xianqian Basin, the Maerguo Formation unconformably overlies Mesozoic sedimentary and granitoid rocks (Fig. 4A). The basal unconformity is overlain by the alluvial lower conglomerates (unit Em_1), which transitions laterally and upward into the fluvial red beds (unit Em_2). Unit Em_2 gradually transitions into the lower fine-grained lacustrine red beds (unit Em_3). Further up section, the upper lacustrine unit (unit Em_4) includes facies (Figs. 4B and 4H) indicative of gravity-flow deposition in a deeper lacustrine environment than unit Em_3, before finally being capped by alluvial upper conglomerates (unit Em_5; see Fig. 4C). The northern margin of the Xianqian Basin is bounded by the north-dipping Xianqian thrust fault, which places pre-Cretaceous granitoid, limestone, and clastic rocks in the north (Figs. 4C and 4D) and Cretaceous volcanic rocks in the northeast (Fig. 4E) in the hanging wall over Eocene red beds of the Maerguo Formation in the footwall. Growth strata are locally present within the Maerguo Formation, suggesting that deposition was contemporaneous with motion on the Xianqian thrust (Fig. 4E).

In the southern Xianqian Basin, the Maerguo Formation unconformably overlies Cretaceous volcanic rocks and Mesozoic sedimentary strata

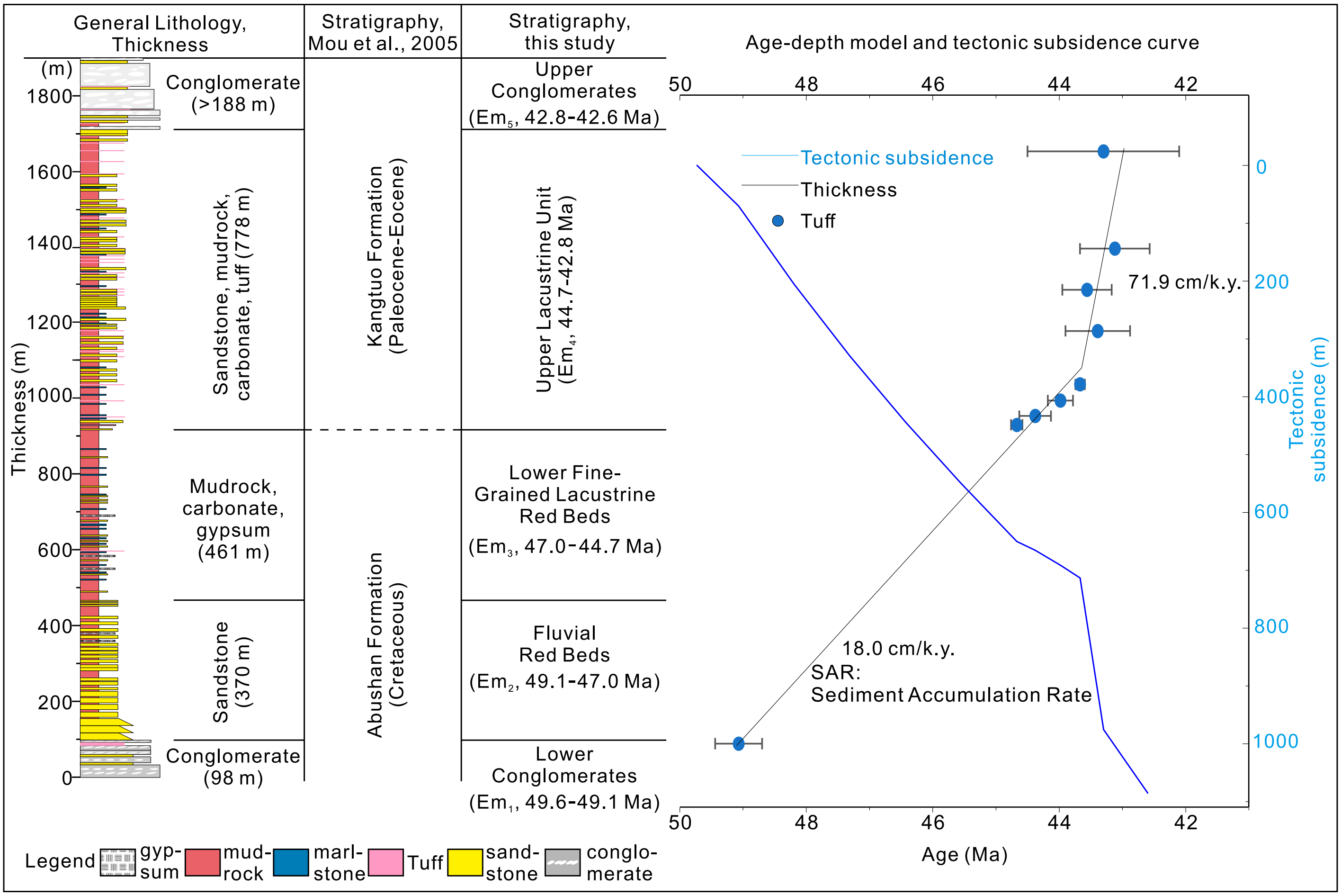

Figure 3. Integrated stratigraphic chart for the Xianqian Basin. The former stratigraphic scheme of the Chinese Geological Survey (Mou et al., 2005) is shown for comparison. The age-depth model and tectonic subsidence curve were plotted based on tuff age points reported in A. Ma (2025, personal comm.).

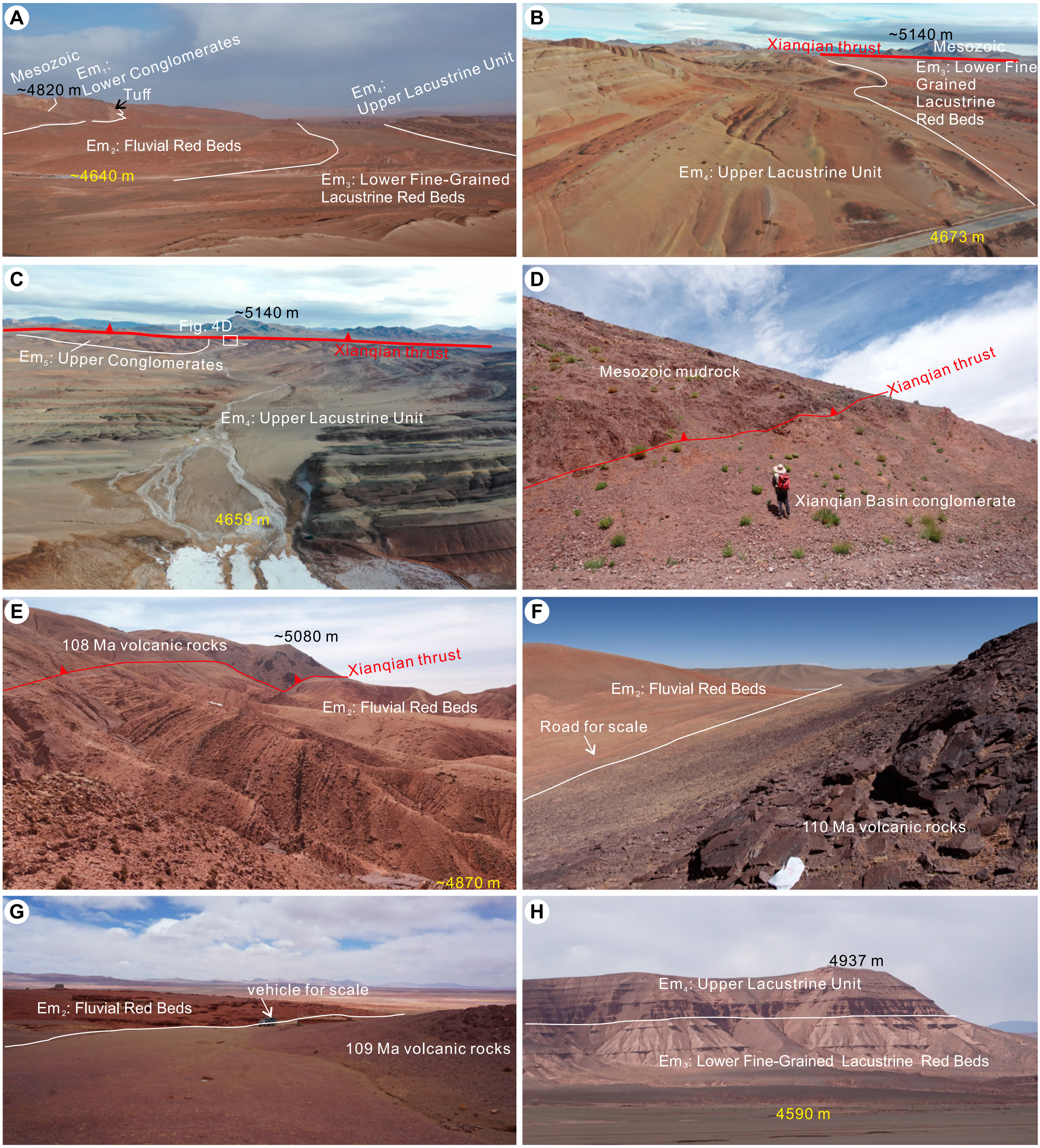

Figure 4. Field photos showing major geologic contacts. (A) Bottom of the Xianqian Basin strata, section N01. View toward the west. (B) Stratigraphic transition from unit Em$_3$ to unit Em$_4$, section N02. View toward the north. (C) Top of Xianqian Basin strata, sections N03 and N04. View toward the north. (D) North-dipping Xianqian thrust juxtaposing Mesozoic mudrock in the hanging wall against the upper lacustrine unit and upper conglomerates in the footwall. View toward the northeast. (E) Circa 108 Ma volcanic rocks thrust over the Xianqian Basin, synchronous with sedimentation of unit Em$_2$ in the footwall, which show growth strata with overturned beds in the proximal footwall, section NE01. View toward the east. (F) Unit Em$_2$ unconformably overlying ca. 110 Ma volcanic rocks, section SE01. View toward the west. (G) Unit Em$_2$ unconformably overlying ca. 109 Ma volcanic rocks, section SW01. View toward the north. (H) Stratigraphic transition from unit Em$_3$ to unit Em$_4$, section S01. The cliff is ~350 m high. View toward the north.

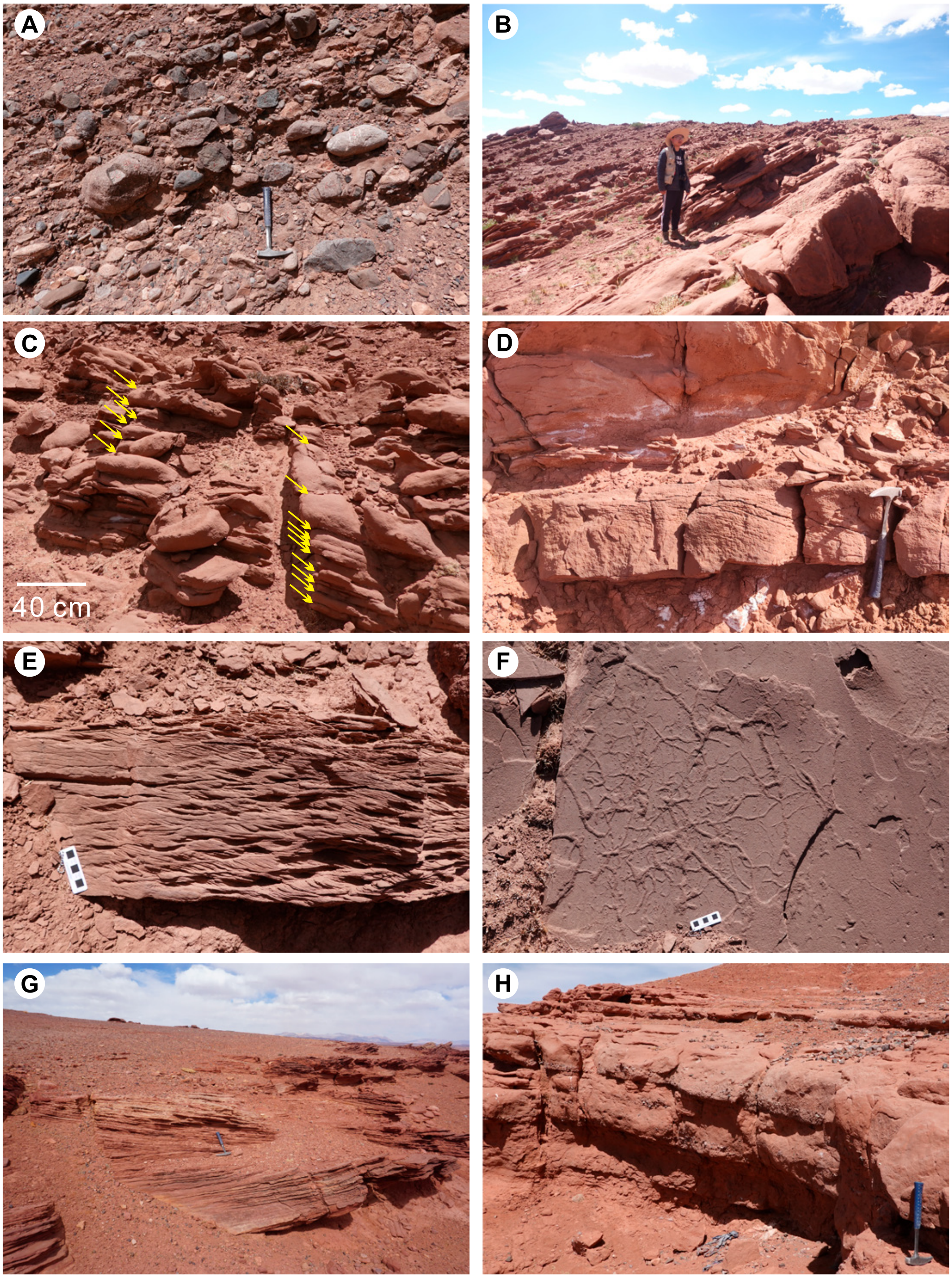

Figure 5. Field photos showing the typical lithofacies in units Em$_1$, Em$_2$, and Em$_3$. (A) Crudely horizontally stratified and clast-imbricated conglomerate (Gchi), unit Em$_1$, section N01. (B) Alternation of red sandstone (Sh, St, Sm, Sb, Sp, and Sr) and mudrock (F), unit Em$_2$, section N01. (C) Sandstone with horizontal stratification (Sh) is organized into multiple beds bounded by finer-grained materials, as indicated by yellow arrows, unit Em$_2$, section N01. (D) Trough cross-bedded sandstone (St) in the overturned unit Em$_2$, section NE01. (E) Fine-grained sandstone with climbing ripples (Sr), unit Em$_2$, section N02. (F) Bioturbated sandstone (Sb) with trace fossil on top, unit Em$_2$, section N01. (G) Planar cross-bedded sandstone in unit Em$_2$, section SW01. (H) Multistory upward-fining sandstone bodies bounded by pebbles at the base, indicative of channel lag deposits in braided rivers, unit Em$_2$, section SE02.

(Figs. 4F and 4G). Unit Em$_1$ is absent; unit Em$_2$, characterized by red sandstone and mudrock, directly overlies the Cretaceous volcanic rocks or Jurassic sedimentary rocks. The contacts between the units within the Maerguo Formation in the southern basin are conformable (Fig. 4H). Unit Em$_5$ also does not crop out in the southern Xianqian Basin.

Below, we describe the sedimentologic features of each stratigraphic unit. The representative lithofacies photos are provided in Figures 5 and 6, and logs of measured sections are provided in Figures 7–10.

4.1.1. Unit Em$_1$: Lower Conglomerates

4.1.1.1. Description. Unit Em$_1$ (lower conglomerates) is 98 m thick in section N01 in the northern Xianqian Basin. This unit consists of an overall fining-upward sequence of boulder to pebble conglomerate with minor sandstone interbeds. In the lower part of section N01, the conglomerates are poorly sorted, with maximum clast sizes reaching ~35 cm along the long axis. Clast size decreases to ~15 cm and sorting improves to moderate in the upper part of the section. The conglomerate is clast-supported, poorly to moderately sorted, and primarily displays crude horizontal stratification (lithofacies code Gch). It commonly exhibits imbrication with long axes oriented transverse to the paleo-

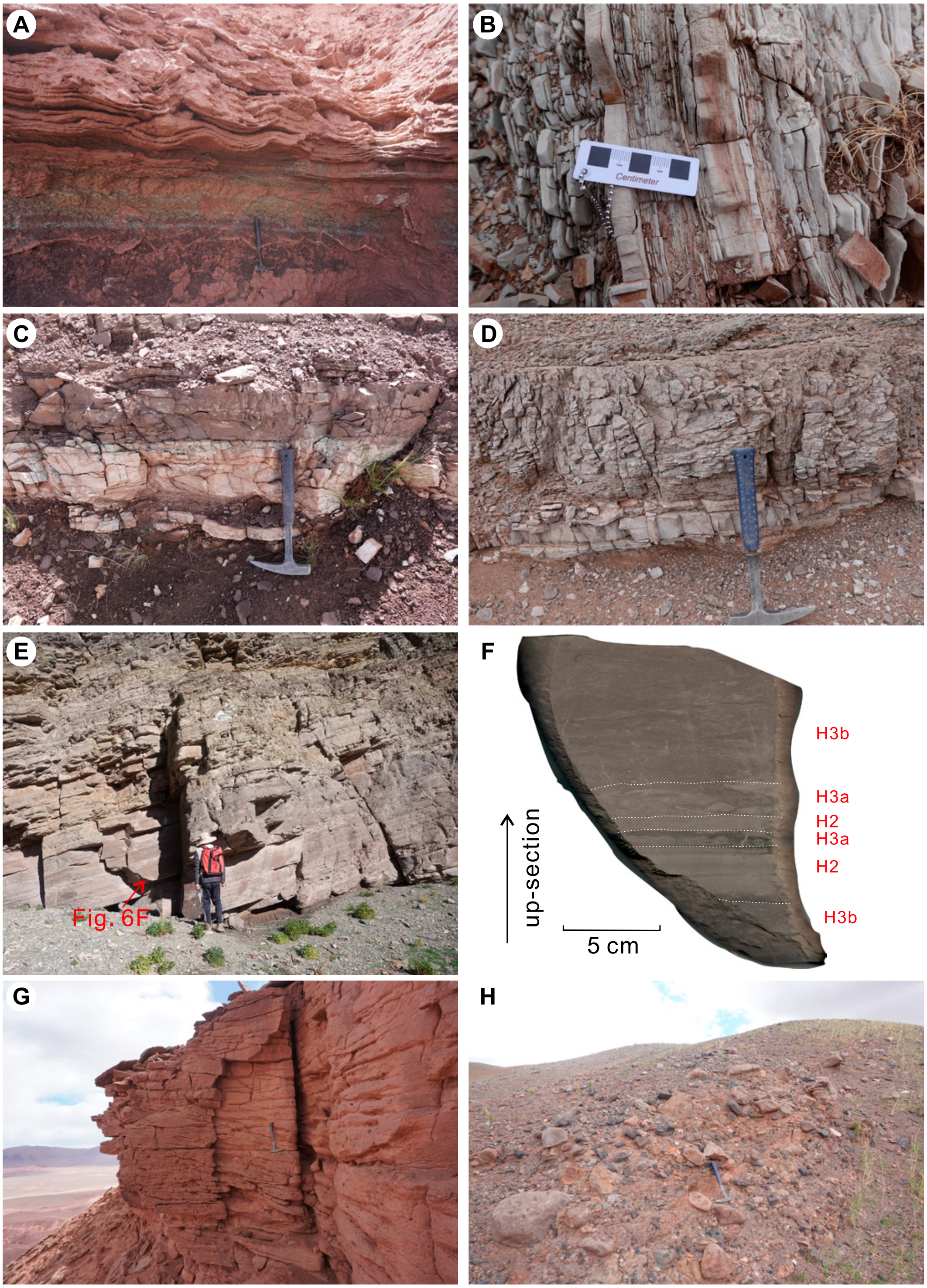

Figure 6. Field photos showing the typical lithofacies in units Em$_3$, Em$_4$, and Em$_5$. (A) Gypsum (Gyp) with structurally deformed laminations, along with green micrite (M) intralayers, unit Em$_3$, section S01. (B) Thinly interbedded micritic carbonate (M), unit Em$_3$, section N01. (C) White-colored tuff (Vt) beneath the sandstone, unit Em$_4$, section N02. (D) Medium-bedded clast-bearing tuffaceous breccia (Vb) overlying the thinly bedded tuff (Vt), unit Em$_4$, section N04. (E) Thickly to thinly bedded tabular gray layers of sandstone and mudrock with good lateral continuity, deposited through sublacustrine gravity flows, unit Em$_4$, section N03. (F) Hybrid event beds with three internal divisions in a sample collected in beds as shown in part E: H2—alternating lighter and darker sands; H3—mud-rich debritic sandstone, where subunit H3b contains more mud than H3a. Interpretation is based on Haughton et al. (2009) and Dodd et al. (2022). (G) Superposition of trough cross-bedded sandstone (St), unit Em$_4$, section S01. (H) Clast-supported massive conglomerate (Gcm), unit Em$_5$, section N03.

flow direction (Gchi; Fig. 5A), while cross-stratified conglomerates (Gt) are relatively rare. The conglomerates are arranged in 1–2-m-thick beds, typically with erosional basal surfaces and finer-grained upper parts. Lenticular beds of massive granular to coarse-grained sandstone (Sm) are locally intercalated. These lithofacies are grouped within (litho)facies association 1 (FA 1).

4.1.1.2. Interpretation. The relatively scarce occurrence of gravity-flow lithofacies (e.g., disorganized Gmm and Gcm) and the abundance of organized conglomerate (Gch, Gchi, and Gt) suggest that most deposition took place in stream flows, likely during flash floods. The spatially localized occurrence of this unit, along with its lateral transition into amalgamated fluvial sandstones, indicates deposition within stream-dominated alluvial fans (Ori, 1982; Wilford et al., 2005; DeCelles et al., 2011). These strata are less likely to have been deposited in more distal braided rivers on the alluvial plain, as the conglomerate clasts are generally poorly sorted, and large-scale cross-stratified sandstone is absent. Based on the southward sediment transport

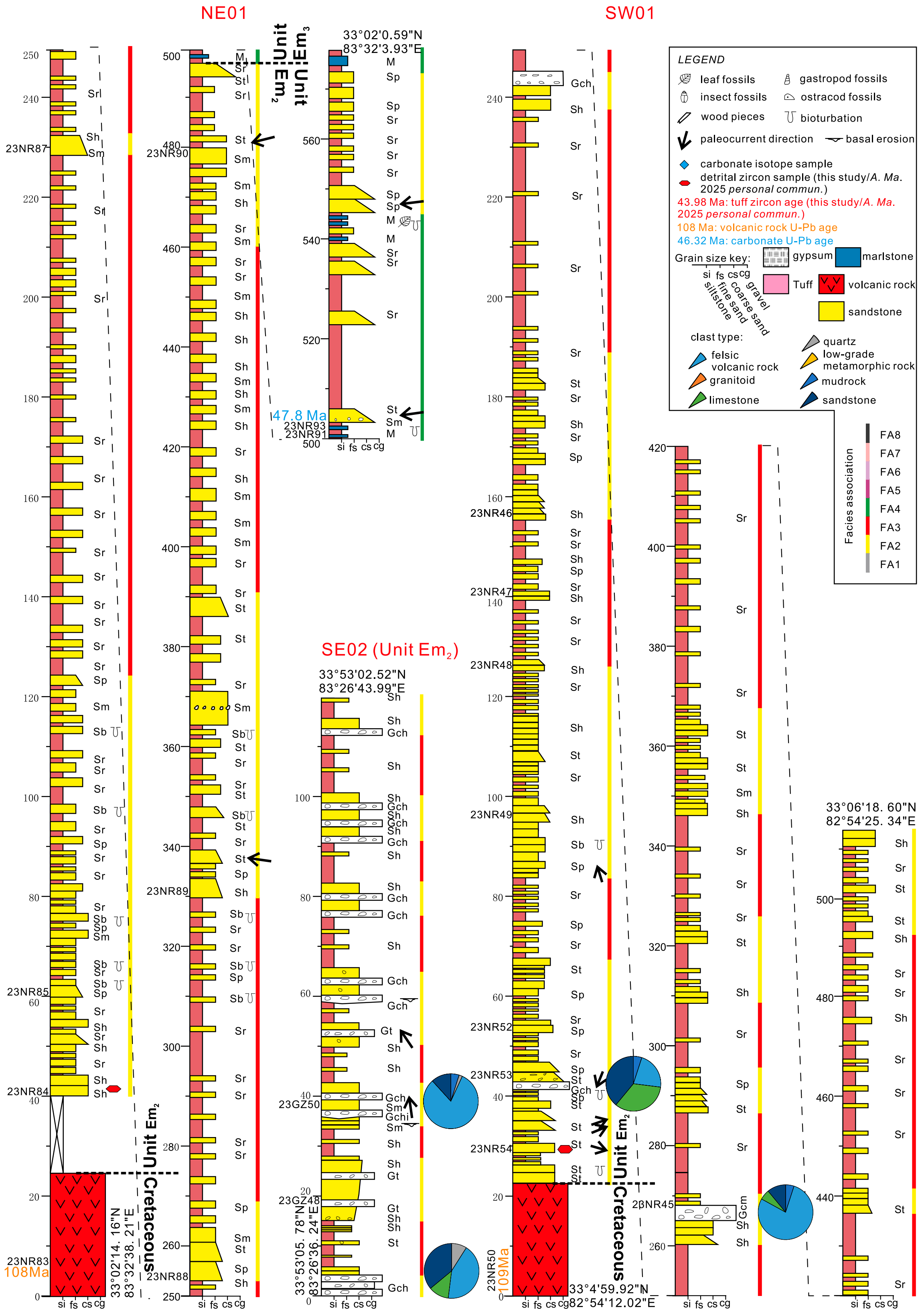

Figure 7. Logs of measured sections NE01, SW01, and SE02. Lithofacies codes refer to Table 1. FA 1—stream-dominated alluvial-fan deposits; FA 2—river channel and levee deposits; FA 3—overbank deposits; FA 4—shallow, muddy playa deposits; FA 5—river channel deposits on delta plain; FA 6—sublacustrine gravity-flow deposits in a delta front to prodelta; FA 7—river channel deposits on delta front; FA 8—gravity flow–dominated alluvial-fan deposits.

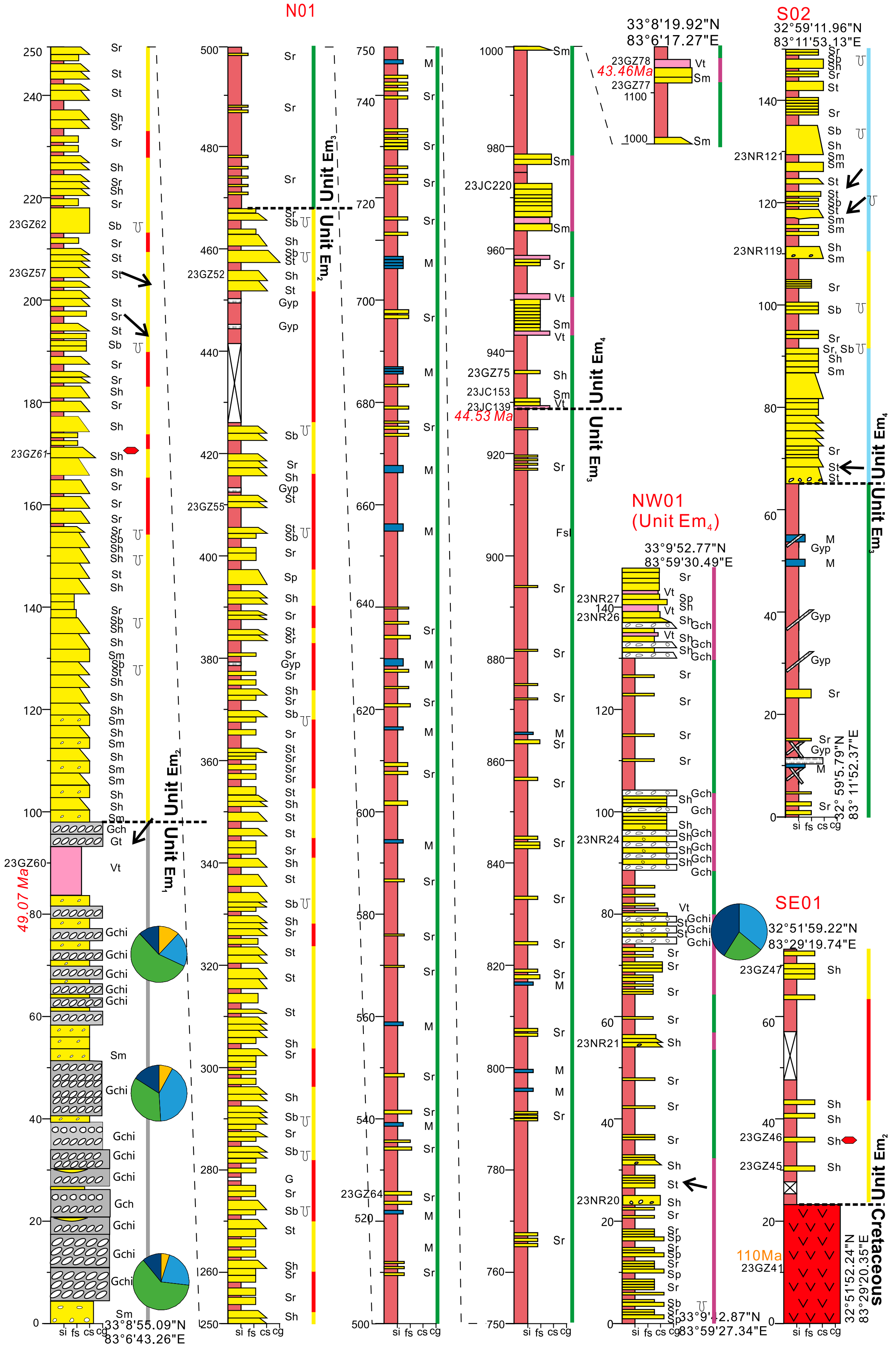

Figure 8. Logs of measured sections N01, S02, SE01, and NW01. Lithofacies codes refer to Table 1. See Figure 7 for legend.

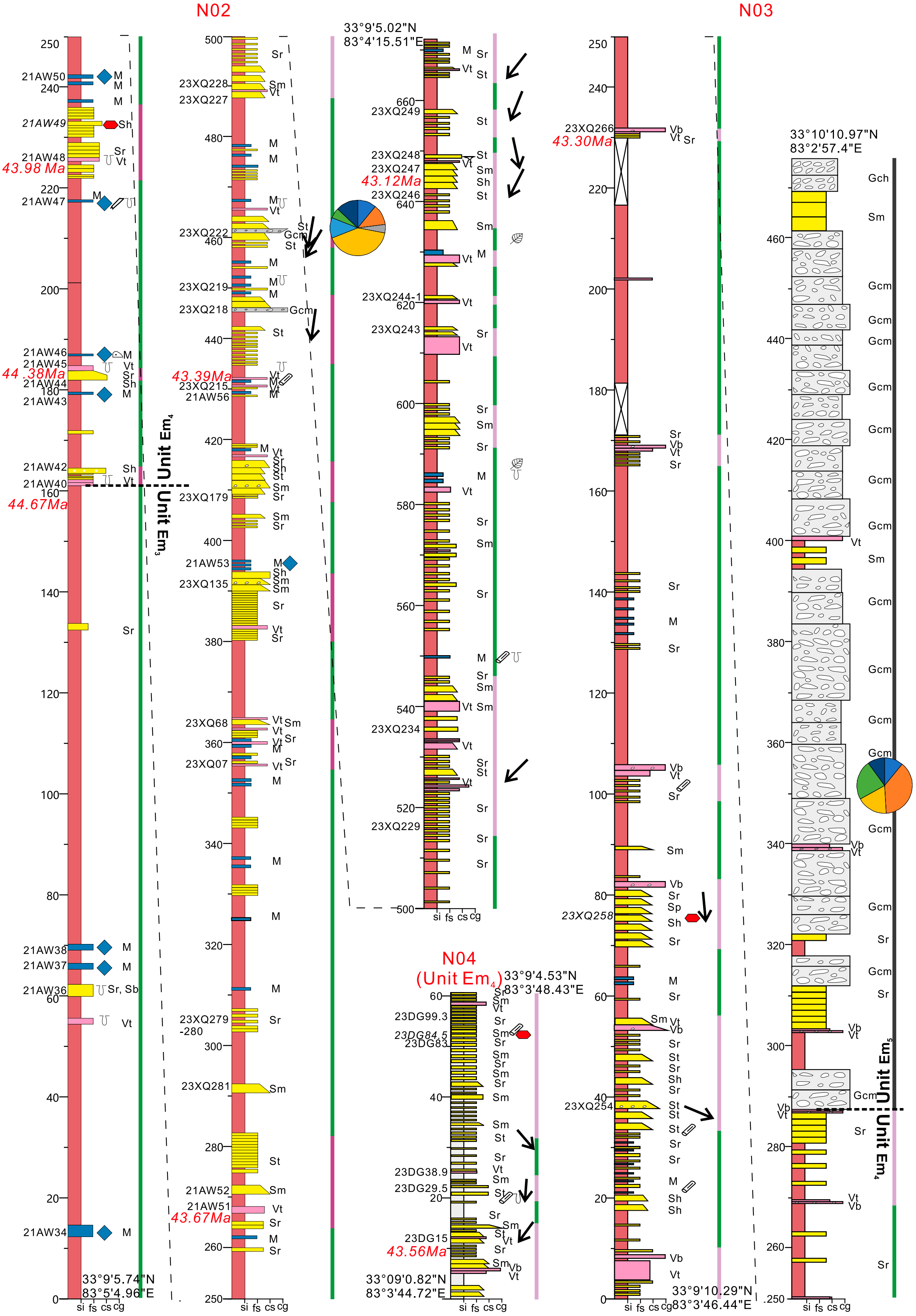

Figure 9. Logs of measured sections N02, N03, and N04. Lithofacies codes refer to Table 1. See Figure 7 for legend.

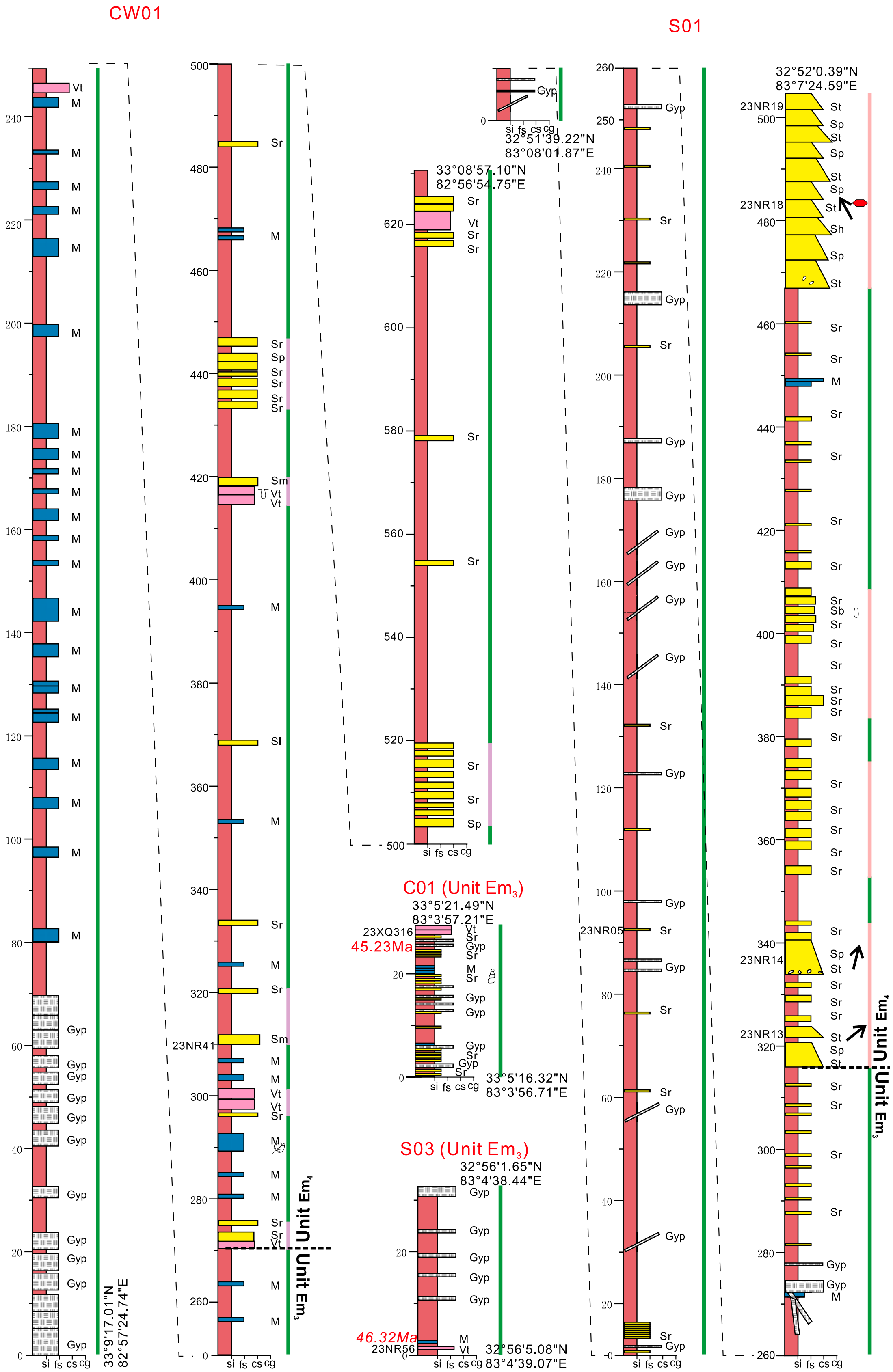

Figure 10. Logs of measured sections CW01, C01, S01, and S03. Lithofacies codes refer to Table 1. See Figure 7 for legend.

inferred from conglomerate clast composition (Table S1), FA 1 in unit Em_1, exposed near the northern margin of the basin, aligns with deposition in alluvial fans that extended southward from high, rugged topography composed of limestone, felsic volcanic rock, sandstone, and low-grade metamorphic rocks within the Qiangtang terrane.

4.1.2 Unit Em_2: Fluvial Red Beds

4.1.2.1. Description. Unit Em_2 (fluvial red beds) is ~370 m thick in section N01, >455 m in section NE01, >50 m in section SE01, >120 m in section SE02, and >510 m in section SW01 (Figs. 7–8). This unit unconformably overlies the late Early Cretaceous volcanic rocks in the sections SE01 and SW01 (Figs. 4F–4G). In section N01, unit Em_2 contains sporadically distributed gypsum fragments within the mudrock at the top and conformably changes into unit Em_3. In contrast, the red beds of unit Em_2 in section NE01 are truncated in the footwall of the Xianqian thrust fault (Fig. 4E). In both sections N01 and NE01, the top of unit Em_2 is marked by a transgressive surface characterized by lacustrine carbonates. In addition, unit Em_2 in section NE01 is characterized by growth strata, with overturned coarse-grained sediments at the bottom and upright fine-grained sediments at the top (Fig. 4E).

Unit Em_2 consists of an upward-fining sequence of alternating red sandstone and mudrock (Figs. 5B) and includes two lithofacies associations (FA 2 and FA 3). FA 2 in unit Em_2 is dominated by medium- to thin-bedded sandstone with horizontal stratification (Sh; Fig. 5C), planar (Sp) and trough cross-stratification (St; Fig. 5D), ripples and climbing ripples (Sr; Fig. 5E), and bioturbation (Sb; Fig. 5F), along with minor mudrock (F). In the northern Xianqian basin, the sandstone in FA 2 is organized into multiple beds bounded by mudrock, as seen in sections N01 and NE01 (Fig. 5C). In the southern Xianqian Basin, sandstone with larger-scale planar cross-stratification (Fig. 5G) in FA 2 mainly occurs as multistory bodies that are bounded by pebble conglomerate, as found in sections SE02 and SW01. The conglomerate is horizontally stratified (Gch) and occasionally imbricated (Gchi) (Fig. 5H) with trough stratification (Gt). Erosive bases can be found at the bottom of some sandstone and conglomerate layers. Overall, sandstone and conglomerate layers in FA 2 are commonly lenticular with river channel geometry along strike. Sandstone and conglomerate in FA 2 become thinner and less common up section. Trace fossil burrows are found both perpendicular and parallel to sandstone layers (Fig. 5F). FA 3 is interbedded with FA 2 and includes mainly mudrock (F) and minor Sr and gypsum fragments (Gyp). FA 3 occurs more common than FA 2 up section.

Paleoflow directions were determined by averaging at least five measurements of dune-scale trough cross-stratification at each site. The results suggest southward paleoflow for unit Em_2 in the sections N01 and NE01, and northward paleoflow in the southern sections SW01 and SE02.

4.1.2.2. Interpretation. Unit Em_2 is interpreted to have been deposited in a fluvial setting, including channel, levee, bars, and overbank deposits. Distinguishing between sand-dominated meandering and braided rivers based solely on outcrop evidence can be challenging, particularly when well-exposed point-bar lateral accretion surfaces, which are characteristic of meandering rivers and oriented perpendicular to the paleoflow direction, are absent (Gibling, 2006; Lyster et al., 2022; Wang et al., 2024).

FA 2 with lithofacies Sh, St, Sp, Gch(i), and Gt is common in fluvial channels. Sh and Gch(i) develop as upper-flow-regime plane beds under very shallow flows; St, Sp, Gt form by the migration of subaqueous sand dunes under unidirectional currents (e.g., Cant and Walker, 1978). Interfaces between multiple 5–20-cm-thick sand beds, characterized by finer-grained materials (Fig. 5C), could be interpreted as lateral accretion surfaces, suggestive of point bars in meandering river systems. However, these fine-grained materials may also occur in bars and overbanks of sandy braided rivers, which would be difficult to differentiate from laterally accreting point bars without detailed paleocurrent work (Miall, 1977; Wang et al., 2024). Multistory upward-fining sandstone bodies bounded by pebbles at their erosive bases (Fig. 5H) are indicative of channel lag deposits in braided rivers. Lithofacies Sr with climbing ripples in FA 2 indicates rapid sediment accretion associated with crevasse-splay deposition or bar-top deposits during waning floods. Compared to FA 2, the increasing appearance of lithofacies Sr and F in FA 3 is associated with overbank deposits. The occurrence of sporadic gypsum fragments within mudrock of FA 3 indicates deposition in arid environments. Unit Em_2 deposits were heavily bioturbated, as suggested by abundant trace fossils.

4.1.3. Unit Em_3: Lower Fine-Grained Lacustrine Red Beds

4.1.3.1. Description. Unit Em_3 (lower fine-grained lacustrine red beds) is ~461 m thick in section N01, >80 m thick in section NE01, >310 m in section S01, >65 m in section S02, >30 m in section S03, ~290 m in section CW01, and >25 m in section C01. This unit includes lithofacies association FA 4, which is dominantly composed of red mudrock, subordinate sandstone, and minor light-gray limestone and gypsum (Figs. 6A and 6B). Sandstone beds are broadly tabular, decimeters to centimeters in thickness, generally fine-grained to very fine-grained (except for a few medium-grained sandstone beds near the tops of the sections), and notable for their abundant climbing ripple cross-stratification. Abundant centimeters-thick gypsum layers and net-like veins are present in the central and southern Xianqian Basin, as seen in sections S01, S02, S03, and CW01, but absent in the northern Xianqian Basin. Overall, the sandstone and gypsum layers are laterally continuous. The sandstones are well laminated, commonly topped by asymmetric ripples (Fig. 5H), and bioturbated in some horizons. The carbonate beds are centimeters in thickness. Plant fragments and gastropods (Fig. 11A) are found in the mudrocks. A few beds of tuff (among which sample 23NR56 from section S03 and sample 23XQ316 from section C01 were dated) are present within unit Em_3.

4.1.3.2. Interpretation. FA 4 in unit Em_3 is interpreted to have been deposited in a shallow, muddy playa environment. Sandstone deposition may have been related to quasi-steady or pulsed discharge of a sandy fluvial system entering an ephemeral lake, whereas the carbonate and gypsum likely formed during periods with insignificant river runoff. The gypsum vein was likely related to postdepositional disruption of original beds. The gastropod *Planorbidae* generally lives within calm water bodies and supports a lake interpretation (Strong et al., 2008). The presence of gypsum suggests a saline environment, especially in the central and southern Xianqian Basin, where gypsum deposition prevailed.

4.1.4. Unit Em_4: Upper Lacustrine Unit

4.1.4.1. Description. Unit Em_4 (upper lacustrine unit) is best exposed in the northern part of the basin, with a thickness of 778 m based on sections N01, N02, N03, N04, CW01, and NW01. Apart from FA 4, which also occurs in unit Em_3 and mainly consists of reddish and gray mudrock (F) with micritic carbonate (M) interlayers throughout unit Em_4, three other lithofacies associations (FA 5–7) were identified. FA 5 in the northern Xianqian Basin includes Sh, Sp, St, Sm, tuff (Vt), Gch(i), and clast-supported massive conglomerate (Gcm). The sandstone and conglomerate are typically restricted to lenticular bodies with erosional bases. The tuffs are mainly white, pink, and reddish in color and dominated by sand-sized volcanic ash grains (Fig. 6C). The sandstone and tuff are locally burrowed. FA 5 is found alternating with FA 4, forming thickening- and coarsening-upward

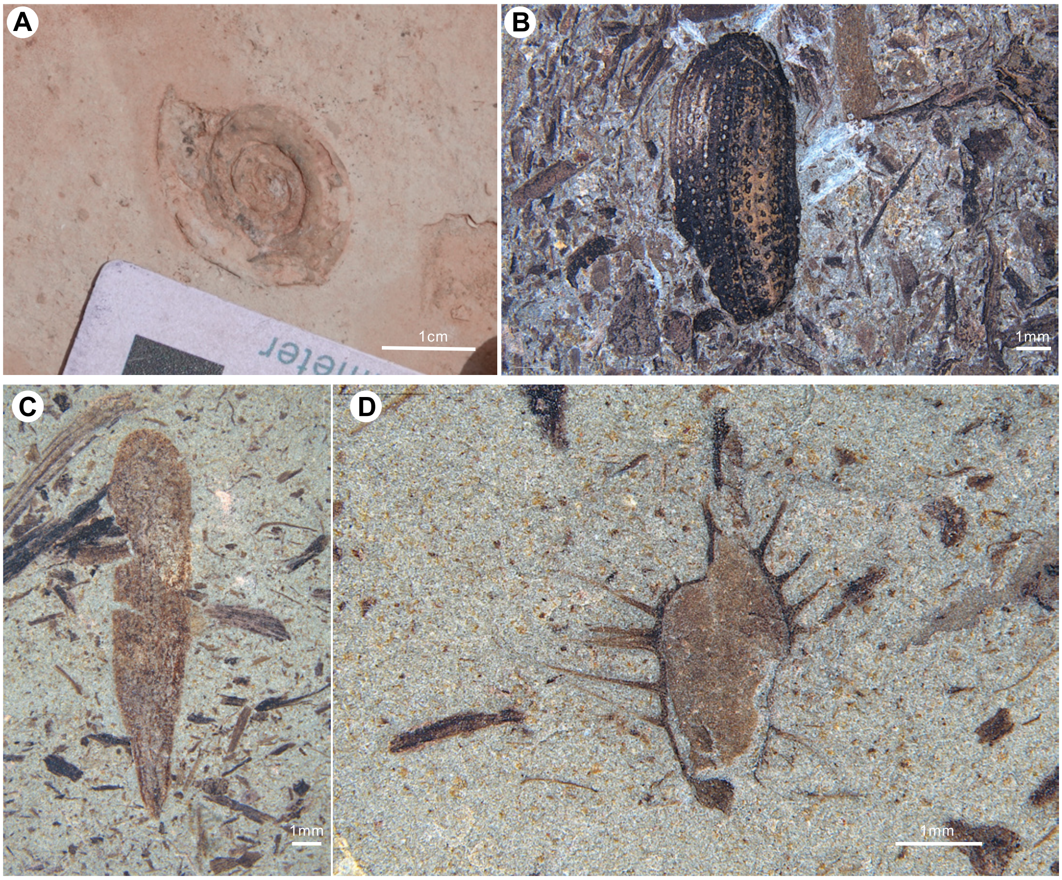

Figure 11. Examples of diverse fossil types and their stratigraphic horizons. (A) Gastropoda: Planorbidae, unit Em$_3$, section C01. (B) Insect fossil of Coleoptera, unit Em$_4$, section N02. (C) Representative leaf morphotype with narrow and elongated shape, unit Em$_4$, section N02. (D) Ceratophyllaceae Gray *Ceratophyllum* sp.? unit Em$_4$, section N02.

packages (up to several meters thick) in the basal 306 m of unit Em$_4$, as seen in sections N01–N03.

FA 6, characterized by tabular beds of sandstone, tuff, and tuffaceous breccia, punctuates the upper 472 m of unit Em$_4$ in the northern basin. These beds are laterally continuous at the kilometer scale. Tuffs (Vt) are similar in color and composition to those in the lower unit Em$_4$. Tuffaceous breccias (Vb) are pink to gray in color and contain mudrock, metamorphic rock, and granitoid clast (Fig. 6D). The sandstones are red to gray in color with lithofacies St, Sp, Sh, Sm, and Sr. Thickly to thinly bedded tabular gray layers of sandstone and mudrock, exhibiting good lateral continuity and upward-fining sequences, are stacked (Fig. 6E). An ideal individual sequence is typically characterized by a progression from clean, structureless, fine- to coarse-grained sandstone (Sm), "banding" of clean sandstone and light-gray mud-rich sandstone (Sm and F), mud-rich structureless sandstone with elongate mud clasts (Sm), to sandstone and mudrock with parallel and ripple laminations, and laminated mudrock (Sr and F) from bottom to top (Fig. 6F), though some lithofacies may be absent in a single bed. Alternating with FA 6, thin to very thinly bedded mudrock (F) and micritic carbonate (M) of FA 4 contain abundant fossilized insects of Coleoptera (Fig. 11B) and plant fragments (Figs. 11C and 11D).

In the southern part of the basin, the scarcity of chronostratigraphic constraints makes it more challenging to correlate sections, but the top ~190 m intervals of sections S01 and S02 feature generally coarser strata that may be correlative to the unit defined as Em$_4$ in the north. These strata consist of medium- to thick-bedded sandstone (FA 7) and interbedded mudrock (FA 4; Fig. 6G), forming an overall upward-coarsening sequence. The sandstone layers in FA 7 are also tabular, laterally continuous over hundreds of meters, and characterized by St (Fig. 6F), Sp, and Sr lithofacies. In certain horizons, the sandstones show heavy bioturbation (Sb). Carbonate and gypsum beds are less common in unit Em$_4$, with only one thinly bedded carbonate layer documented in section S01.

Paleoflow directions were reconstructed using cross-bedding measurements at different locations, with at least five measurements averaged per site. The results indicate a southward paleoflow in the northern part of the basin and a northward paleoflow in the southern part of the basin.

4.1.4.2. Interpretation. The red strata containing FA 4 and FA 5 in the lower 306 m are interpreted as having been deposited in a deltaic plain, influenced by both river discharge and lake-level fluctuations. The mudrock and carbonate in FA 4 were likely deposited during periods of reduced river clastic input, coinciding with lake-level highstands. In contrast, the well-organized sandstone and conglomerate in FA 5 likely represent cut-and-fill deposition in unidirectional river channels on the deltaic plain, while the less common poorly organized conglomerate and sandstone beds may reflect deposition during flood events.

In the upper 472 m of unit Em$_4$, the tabular gray layers with lateral continuity, comprising structureless sandstone and laminated mudrock in FA 6, are interpreted as gravity-flow deposits in a delta-front to prodelta setting of a relatively deep lacustrine environment. These deposits resemble hybrid event beds, which are deposited by flows exhibiting "mixed behavior," resulting in complex successions of sandstone and mudrock (Baas et al., 2011; Stevenson et al., 2020). The Sm at the base represents the H1 of the hybrid event beds; the banded sandstone represents H2, which formed through bed-form development under transitional flow conditions; the mud-rich sandstone with mud clasts is typical of hybrid event beds and represents H3, with

TABLE 2. SUMMARY OF TUFF AND CARBONATE AGES FROM THE XIANQIAN BASIN

Tuff sample no.	Lithology	Unit	Location	Global positioning system location	Age (Ma)	Data source
23XQ316	Tuff	Em$_3$	Section CW01	33.0893°N, 83.0659°E	45.23 ± 0.40 ($n = 15$, MSWD = 0.87)	This study
23NR93	Carbonate	Em$_3$	Section NE01	33.0347°N, 83.5373°E	47.8 ± 5.1 ($n = 35$, MSWD = 7.4)	This study
23NR56	Tuff	Em$_3$	Southern Xianqian Basin	32.9347°N, 83.0775°E	46.32 ± 0.54 ($n = 15$, MSWD = 2.4)	A. Ma (2025, personal commun.)
23GZ60	Tuff	88 m,[†] Em$_1$	Section N01	33.1476°N, 83.1112°E	49.07 ± 0.37 ($n = 15$, MSWD = 1.1)	A. Ma (2025, personal commun.)
23JC139	Tuff	930 m,[†] Em$_4$	Section N01	33.1393°N, 83.1068°E	44.53 ± 0.70 ($n = 15$, MSWD = 3.3)	A. Ma (2025, personal commun.)
23GZ78	Tuff	1016 m,[†] Em$_4$	Section N01	33.1389°N, 83.1048°E	43.46 ± 0.80 ($n = 13$, MSWD = 2.1)	A. Ma (2025, personal commun.)
21AW40[*]	Tuff	706 m,[†] Em$_4$	Section N02	33.1503°N, 83.0819°E	44.67 ± 0.18 ($n = 4$, MSWD = 0.052)	A. Ma (2025, personal commun.)
21AW45	Tuff	953 m,[†] Em$_4$	Section N02	33.1502°N, 83.0816°E	44.38 ± 0.25 ($n = 22$, MSWD = 3.5)	A. Ma (2025, personal commun.)
21AW48	Tuff	994 m,[†] Em$_4$	Section N02	33.1504°N, 83.0806°E	43.98 ± 0.20 ($n = 22$, MSWD = 2)	A. Ma (2025, personal commun.)
21AW51[*]	Tuff	1037 m,[†] Em$_4$	Section N02	33.1502°N, 83.0783°E	43.67 ± 0.15 ($n = 4$, MSWD = 0.38	A. Ma (2025, personal commun.)
23XQ215	Tuff	1178 m,[†] Em$_4$	Section N02	33.1509°N, 83.0779°E	43.39 ± 0.51 ($n = 23$, MSWD = 2.1)	A. Ma (2025, personal commun.)
23XQ247	Tuff	1395 m,[†] Em$_4$	Section N02	33.1387°N, 83.1065°E	43.12 ± 0.55 ($n = 8$, MSWD = 0.63)	A. Ma (2025, personal commun.)
23XQ266	Tuff	1652 m,[†] Em$_4$	Section N03	33.1589°N, 83.0644°E	43.30 ± 1.20 ($n = 13$, MSWD = 8.2)	A. Ma (2025, personal commun.)

Note: MSWD—mean square of weighted deviates.

[*] Zircons from these two tuff samples were dated with the chemical abrasion–isotope dilution–thermal ionization mass spectrometry (CA-ID-TIMS) method, and those from other tuff samples were dated with secondary ion mass spectrometry (SIMS).

[†] Sample horizon at the composite section on Figure 3.

subunit H3b containing more mud than H3a; the thin, graded sandstone and mudrock with common parallel and ripple lamination represent H4, which is related to low-density flows in the turbulent wake; and the mudrock cap represents H5, which is formed by suspension fall-out (Haughton et al., 2009; Hussain et al., 2020; Dodd et al., 2022). The common association of these beds with lithofacies Vt and especially Vb suggests that the influx of coarse-grained deposits may have been associated with syndepositional volcanism, with the presence of volcaniclastic breccia indicating nearby volcanic eruptions.

FA 7 in the southern Xianqian Basin (sections S01 and S02), characterized by medium- to thick-bedded layers of St, Sp, and Sh, was likely deposited through tractional flows in distributary channels in a delta front. The upward-coarsening packages probably represent progradational deltaic sequences in shallow lakes (e.g., Bohacs et al., 2003). The red siltstones (F) and bioturbated sandstone (Sb) within FA 4 represent fine-grained overbank deposits on delta plains. The carbonate bed within FA 4 was likely deposited during a lake-level highstand, when clastic detrital input was reduced.

4.1.5. Unit Em5: Upper Conglomerates

4.1.5.1. Description. Unit Em$_5$ (upper conglomerates) is >188 m in thickness and only present in section N03 in the northern Xianqian Basin. It includes FA 8, which is dominated by boulder to pebble conglomerates, with local occurrences of sandstone, mudrock, and tuff beds. The conglomerate is clast-supported and generally massive (Gcm; Fig. 6H). Clasts reach up to 40 cm in diameter, are poorly sorted, and are moderately rounded at the base of the unit. Moving up section, the conglomerate becomes more organized, exhibiting horizontal stratification (Gch). Clast size decreases upward to pebbles that are better rounded and better sorted than boulders and pebbles below. The conglomerates are interbedded with 10–50-cm-thick beds of sandstone (Sm), tuff (Vt), and red mudrock (F).

4.1.5.2. Interpretation. FA 8 in unit Em$_5$ is interpreted as having been deposited in a gravity flow–dominated alluvial-fan environment. Compared to FA 1 in unit Em$_1$, the massive conglomerate occurs more frequently in FA 8, and the clasts are larger in size overall. The Gcm and Sm lithofacies indicate deposition by high-density debris flows, while Gch may represent sieve deposits on an alluvial fan.

4.2. Chronostratigraphic Controls

Zircon U-Pb dating in this study suggests the volcanic rocks bounding the Xianqian Basin are late Early Cretaceous in age. In sections SW01 and SE01, the felsic volcanic rocks unconformably underlying the Maerguo Formation yielded zircons with weighted mean U-Pb ages of 108.8 ± 2.6 Ma ($n = 19$, MSWD = 6.2, sample 23NR50) and 110.0 ± 1.7 Ma ($n = 18$, MSWD = 1.3, sample 23GZ41), respectively (Figs. S1A–S1B). In section NE01, the felsic volcanic rock in the hanging wall yielded a zircon U-Pb age of 108.1 ± 1.8 Ma ($n = 20$, MSWD = 4.2, sample 23NR83; Fig. S1C).

The age of the Maerguo Formation was determined through zircon U-Pb dating of tuff samples and carbonate U-Pb dating (Table 2), from both this study and from A. Ma (2025, personal commun.). In this study, the tuff sample 23XQ316 from unit Em$_3$, located at the top of section CW01, yielded a weighted mean zircon U-Pb age of 45.2 ± 0.4 Ma ($n = 15$, MSWD = 0.87; Fig. S1D). In section NE01, the carbonate sample 23NR93 from unit Em$_3$ yielded a lower-intercept carbonate U-Pb age at 47.8 ± 5.1 Ma ($n = 35$, MSWD = 7.4) on the Tera-Wasserburg plot (Fig. S1E). For sedimentary rocks in other sections that were not dated with tuff zircon or carbonate U-Pb methods, stratigraphic correlation was based on geologic mapping, lithology, and sedimentary facies.

4.3. Sediment Provenance Analysis

4.3.1. Modal Sandstone Petrology

Twenty-six sandstone samples from unit Em$_2$ in both the northern and southern Xianqian Basin, eight sandstone samples from units Em$_3$–Em$_4$ in the southern Xianqian Basin, and one sandstone sample in the lowermost unit Em$_3$ (23GZ64) in the northern Xianqian Basin are rich in quartz grains and plot mostly in the feldspatho-litho-quartzose field of the quartz-feldspar-lithics (QFL) diagram (Fig. 12), following the classification scheme of Garzanti (2019). The lithic fragments are dominated by felsic volcanic rocks and limestone, with subordinate and varying proportions of slate, phyllite, and schist (Fig. 12).

In the northern Xianqian Basin (sections N01–N04), 38 samples from unit Em$_4$ and uppermost unit Em$_3$ record a major change in provenance compared to unit Em$_2$ (Fig. 12). From unit Em$_2$ to unit Em$_3$, there is an increase in feldspar and lithic fragments at the expense of quartz, and an increase in metamorphic fragments at the expense of sedimentary fragments. Overall, higher in the stratigraphic level, there is a greater abundance of schist fragments and plutonic fragments. Unit Em$_4$ in section NW01 and one sample (23NR41) from unit Em$_3$ in section CW01, both located in the northwest Xianqian Basin, show similar quartz content but a higher concentration of limestone fragments compared to sections N01–N04. This indicates a provenance variation along strike along the northern margin of the Xianqian Basin.

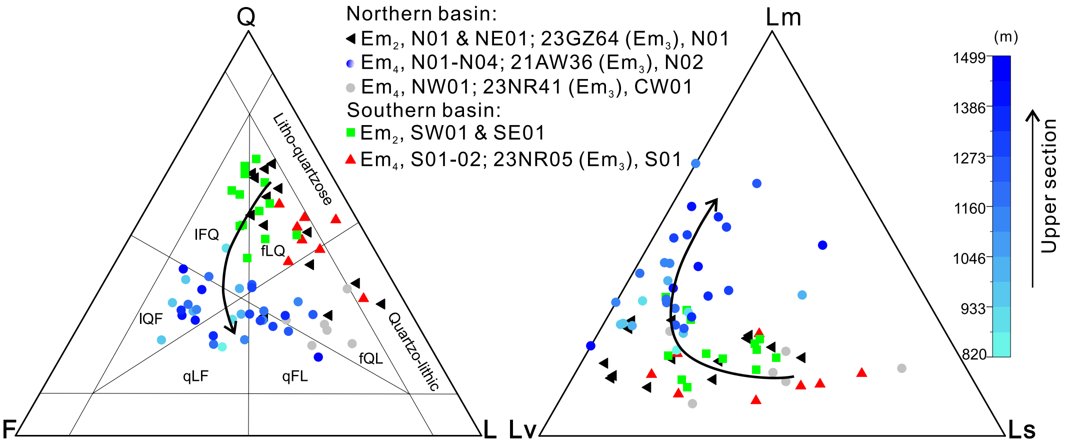

Figure 12. Ternary diagram showing the sandstone petrography in QFL plot with sandstone classification scheme after Garzanti (2019). Q—quartz; F—feldspar; L—lithic fragments (Lv—volcanic; Ls—sedimentary; Lm—metamorphic); fLQ—feldspatho-litho-quartzose; fQL—feldspatho-quartzo-lithic; qFL—quartzo-feldspatho-lithic; lFQ—litho-feldspatho-quartzose; lQF—litho-quartzo-feldspathic; qLF—quartzo-lithofeldspathic; qFL—quartzo-feldspatho-lithic.

4.3.2. Conglomerate Clast Counts

Clasts in conglomerate were counted at 10 sites throughout the entire stratigraphic thickness of the Maerguo Formation (Figs. 7–10). In unit Em_1 of the Maerguo Formation, clasts are predominantly composed of limestone (35%–62%, averaging 51%), felsic volcanic rock (20%–41%, averaging 28%), sandstone (11%–16%, averaging 13%), and low-grade metamorphic rock (5%–12%, averaging 8%). Metamorphic clasts are largely absent in unit Em_2 along the southern margin of the basin and in unit Em_4 in section NW01, where the clasts are dominated by felsic volcanic rock (22%–83%, averaging 52%), sandstone (11%–41%, averaging 29%), and limestone (0%–34%, averaging 15%), with insignificant amounts of quartz and mudrock. In contrast, single-site clast counts of unit Em_4 in section N02 and unit Em_5 in section N03 revealed significant proportions of low-grade metamorphic clasts (41% and 18%, respectively), granitoid (12% and 38%, respectively), mudrock (11% at both sites), sandstone (13% and 10%, respectively), and limestone (6% and 23%, respectively), with quartz (5%) and felsic volcanic rock (12%) present only in unit Em_4.

4.3.3. Detrital Heavy Minerals

The heavy mineral content in units Em_2 and Em_3 in the entire Xianqian Basin and unit Em_4 in the southern Xianqian Basin ranges between 0.3% and 2.1% with an average of 0.9%. The transparent heavy mineral suite accounts for 4%–68% (with an average of 28%) in volume and consists of zircon, tourmaline, apatite, garnet, rutile, titanite, epidote, and rare grains of amphibole and clinopyroxene. In the biplot of heavy mineral data, these samples plotted mainly in the first and fourth quartiles, indicating dominance of zircon, rutile, tourmaline, and titanite, among others (Fig. 13). The ZTR index varies between 27 and 78 with an average of 58.

Unit Em_4 in the northern Xianqian Basin yielded notably different heavy mineral characteristics, with a higher proportion of transparent heavy minerals compared to strata below the unit and elsewhere in the Xianqian Basin. The heavy mineral content varies between 0.3% and 4.5% (average of 2.5%), and the transparent heavy mineral suite accounts for 33%–90% (average of 64%). Compared to that of unit Em_2 underneath, the transparent heavy mineral suite is characterized by an increasing content of amphibole at the expense of apatite, zircon, tourmaline, and rutile (Fig. 13). Within unit Em_4 in the northern Xianqian Basin, the ZTR index declines upward from 38 to insignificant values, while amphibole comprises up to 94% in the uppermost unit Em_4.

4.3.4. Detrital Zircon U-Pb Age Spectra

Figure 14 presents kernel density estimation (KDE), probability density plot (PDP), and histogram (bin width 10 Ma) representations of the detrital zircon U-Pb ages from sandstones in the Xianqian Basin and potential source terranes. KDE is preferred here for detrital provenance interpretation due to its solid theoretical underpinnings and its ability to avoid the double-smoothing effect and artificial peaks found in PDPs, resulting in more accurate probability density estimates (Vermeesch, 2012). Three sandstone samples in unit Em_2, including one from section NE01 (23NR84) in the northern Xianqian Basin and two (23GZ46 in section SE01, 23NR54 in section SW01) in the southern basin, and one sandstone sample (23NR18) in unit Em_4 from the southern Xianqian Basin share similar zircon U-Pb age spectra, including an age peak ca. 110 Ma (Fig. 14). Older peaks at 150 Ma, 220 Ma, 425 Ma, 860 Ma, 1870 Ma, and 2500 Ma are present in 23NR84, 23GZ46, and 23NR18 but are insignificant in 23NR54 in the southwestern Xianqian Basin (Fig. 14). Samples 23NR84, 23GZ46, and 23NR18 contained a few scattered ages between 60 Ma and 100 Ma.

In the northern Xianqian Basin, detrital zircons within unit Em_2 sandstone (23GZ61 in section N01) are characterized by multiple U-Pb age peaks at 115 Ma, 160 Ma, 220 Ma, 270 Ma, 1000 Ma, 1850 Ma, and 2500 Ma (A. Ma, 2025, personal commun.), which are very similar to those of 23NR84 in the northeast Xianqian Basin along strike (Fig. 14). In contrast, samples from unit Em_4 (21AW49 in section N02, 23DG84.5 in section N04, and 23XQ258 in section N03) in the northern Xianqian Basin are characterized by a single dominant age peak at 160–150 Ma (A. Ma, 2025, personal commun.; Fig. 14). A granitoid clast (sample 23XQ271) in unit Em_5 yielded a weighted mean zircon U-Pb age of 161.5 ± 2.7 Ma ($n = 19$, MSWD = 2.8; see Fig. S1F).

To investigate potential sources for the basin, we analyzed several samples outside of the basin. A sandstone sample (23NR60) from Jurassic strata to the north of the Xianqian Basin yielded detrital zircons with U-Pb ages peaks at 200 Ma, 270 Ma, 520 Ma, and 1130 Ma, multiple small peaks between 550 Ma and 1040 Ma, and other insignificant small peaks (Fig. 14). The maximum depositional age of this Jurassic sandstone is constrained by the three youngest detrital zircons dated: 179 ± 4 Ma, 181 ± 3 Ma, 188 ± 4 Ma. One sample (23TG01) from the Cretaceous Abushan Formation continental red bed and one sample (23TG14) previously mapped as the Upper Triassic Tinggongcuo Formation (Yue et al., 2006) yielded similar detrital zircon U-Pb age spectra, both of which displayed scattered multiple age peaks at 300–200 Ma and 1000–500 Ma, along with subordinate peaks at 1840 Ma and 2500 Ma (Fig. 14). The youngest age peak in both stratigraphic units is Late Jurassic (23TG01 at ca. 160 Ma and 23TG14 at ca. 145 Ma). The existence of abundant zircons

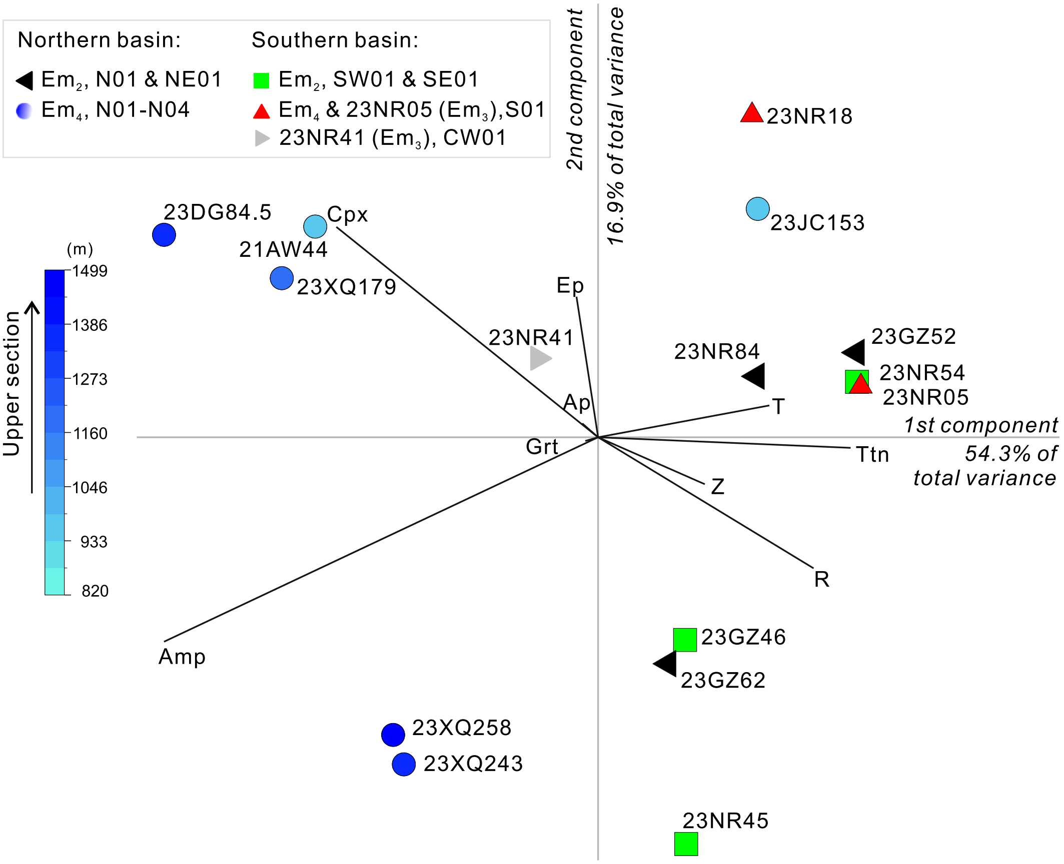

Figure 13. Heavy mineral compositional biplot. The length of each ray is proportional to the variance of the corresponding element in the dataset; if the angle between two rays is close to 0°, 90°, or 180°, then the corresponding variables are directly correlated, uncorrelated, or inversely correlated, respectively (Gabriel, 1971). Ap—apatite; Cpx—clinopyroxene; Grt—garnet; Ttn—titanite; Ep—epidote; Amp—amphibole; Z—zircon; T—tourmaline; R—rutile.

with ages near the Jurassic-Cretaceous boundary suggests a Cretaceous or younger depositional age for the so-called Tinggongcuo Formation. In addition, 350 Ma, 390 Ma, and 435 Ma peaks in 23TG01 are insignificant in 23TG14, which instead exhibits a prominent 450 Ma peak (Fig. 14).

4.4. Tectonic Subsidence of the Xianqian Basin

The reconstructed tectonic subsidence curve (Fig. 3) suggests the Xianqian Basin experienced ~710 m of tectonic subsidence from ca. 50 Ma to 43 Ma, with a relatively low tectonic subsidence rate at ~0.1 mm/yr. Then, tectonic subsidence accelerated to ~0.7 mm/yr, and the basin subsided an additional 260 m by ca. 43.3 Ma (Fig. 3). Finally, tectonic subsidence decelerated back to <0.2 mm/yr with a total of 110 m of tectonic subsidence by ca. 42.6 Ma (Fig. 3).

5. DISCUSSION

5.1. Sediment Provenance Interpretation

The southern Xianqian Basin records no significant provenance changes throughout the depositional history of the Maerguo Formation, whereas the northern Xianqian Basin shows a provenance shift between units Em_1–Em_2 and units Em_4–Em_5. Units Em_1, Em_2, and Em_4 in the southern Xianqian Basin exhibit a recycled orogen provenance (Dickinson, 1985; Garzanti et al., 2007), as the sandstones from these units are dominated by quartz and lithic fragments, with the latter primarily consisting of felsic volcanic and sedimentary fragments (Fig. 12). Conglomerate compositions generally support this interpretation, with clasts predominantly composed of sandstone, volcanic rocks, limestone, and minor amounts of quartz and mudrock. The dominance of zircon, tourmaline, apatite, garnet, and rutile in the heavy mineral assemblage, with an average ZTR index of 58, also supports the recycled provenance interpretation. In certain stratigraphic levels of sections SE01 and SW01, volcanic clasts dominate, likely recycled from Cretaceous volcanic rocks exposed farther to the south. The youngest detrital zircon U-Pb ages, peaking at ca. 110 Ma, further confirm a contribution from Cretaceous volcanic rocks. The presence of multiple older age peaks at ca. 160 Ma, 220 Ma, 270 Ma, 1000 Ma, 1850 Ma, and 2500 Ma suggests recycling of materials from pre-Cretaceous sedimentary rocks that were exposed around the basin during deposition (Li et al., 2017; Ma et al., 2017).

Compared to units Em_2–Em_3, units Em_4–Em_5 in the northern Xianqian Basin exhibit a significant change in detrital composition, characterized by increased feldspar content and decreased quartz content in sandstones (Fig. 12). This shift is typical of rocks derived from a transitional to dissected magmatic arc (Dickinson, 1985). The presence of granitoid fragments, a distinct detrital zircon U-Pb age peak at ca. 150 Ma in sandstone, ca. 162 Ma granitoid clasts in conglomerate, and the significant amount of hornblende in the heavy mineral assemblage further support this interpretation. However, the abundance of low-grade metamorphic rock, mudrock, sandstone, volcanic rock, and limestone fragments in both sandstone and conglomerate points to a recycled orogen source. U-Pb age signals of other contributions may have been masked by the prominence of granitoid rocks, which are rich sources of sand-sized zircon (Garzanti and Andò, 2019). Based on paleocurrent measurements, we suggest the major source of sediment was the Late Jurassic granitoids located to the north of the basin, which is further supported by the abundance of amphibole and clinopyroxene in heavy minerals against the

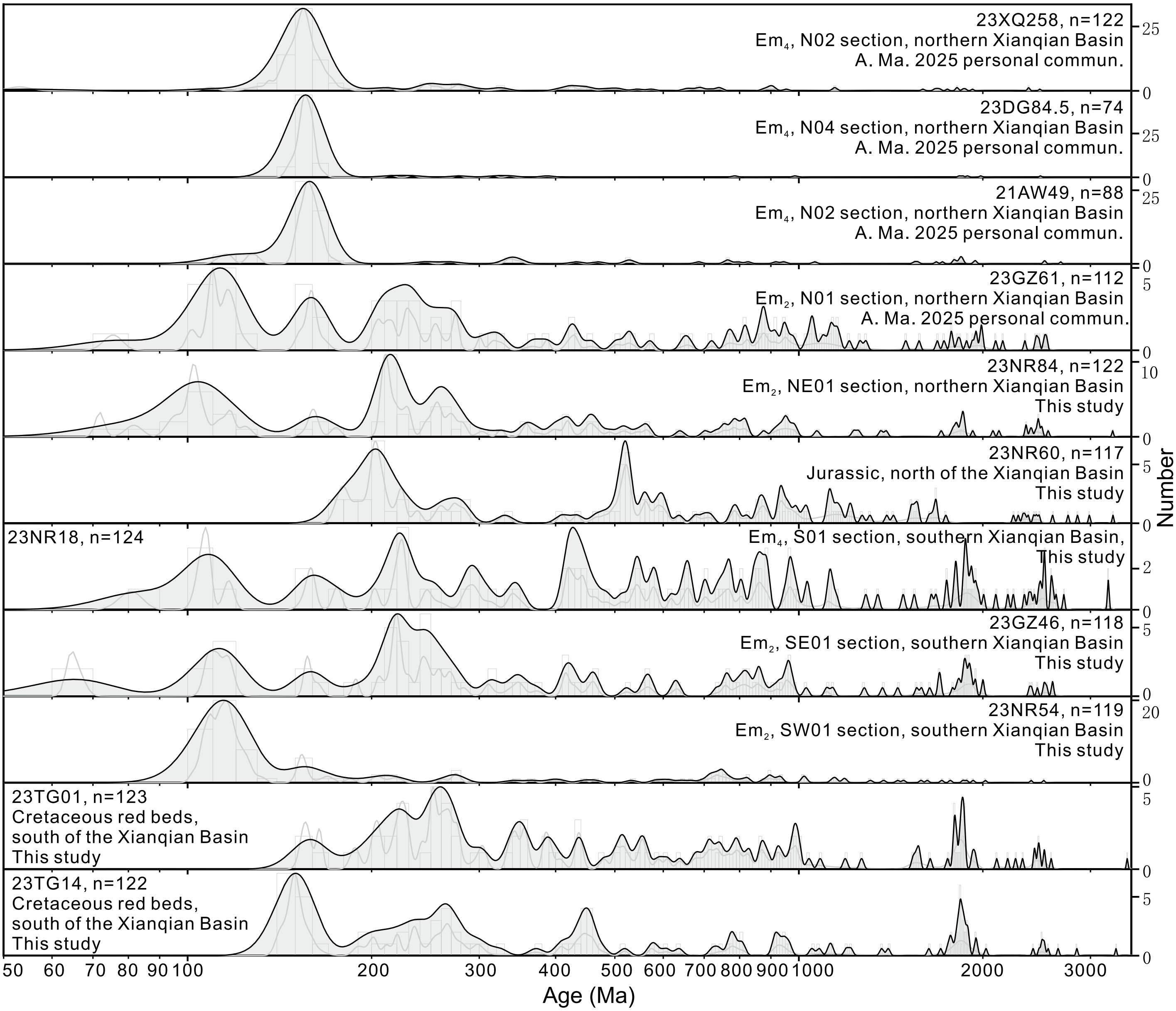

Figure 14. Kernel density estimation (KDE; black curve, filled, and bandwidth 50 Ma), probability density plot (PDP; gray curve), and histograms (bin width 10 Ma) of the detrital zircon U-Pb ages from the sandstones of potential provenance and from the sandstones in the Xianqian Basin.

percentage of 166–143 Ma detrital zircon ages within the Maerguo Formation (Fig. S3). This provenance change, documented in the northern Xianqian Basin at ca. 45 Ma, implies more rapid unroofing of the source area to the north of the basin, or the exhumation of granitoids that were previously unexposed.

5.2. Basin Architecture and Paleogeography

The stratigraphy, sedimentology, and provenance analyses demonstrate that the oval-shaped Xianqian Basin is dominated by coarse-grained facies along the margins and fine-grained lacustrine facies in the center. Figure 15 depicts a tentative lithostratigraphic correlation based on our measured sections. We suggest that the Xianqian Basin was filled by three distinct depositional systems: an initial lower alluvial-fluvial system with bidirectional paleoflows, coinciding with north-south shortening that induced the development of growth strata in the northern basin; a medial lacustrine system into which marginal deltas systems prograded, again characterized by bidirectional provenance; and an upper alluvial system in the northern basin, primarily sourced from granitoid and metamorphic rocks in the hanging wall of the Xianqian thrust.

The basin fill exhibits an overall upward fining followed by a coarsening grain-size trend, resembling the classic “lacustrine sandwich” pattern, which is often considered a hallmark of extensional basins (Schlische, 1992). However, the presence of the syndepositional north-dipping Xianqian thrust and growth strata in the north suggests that the Xianqian Basin developed in a contractional setting. This contraction did not significantly affect the southern Xianqian Basin,

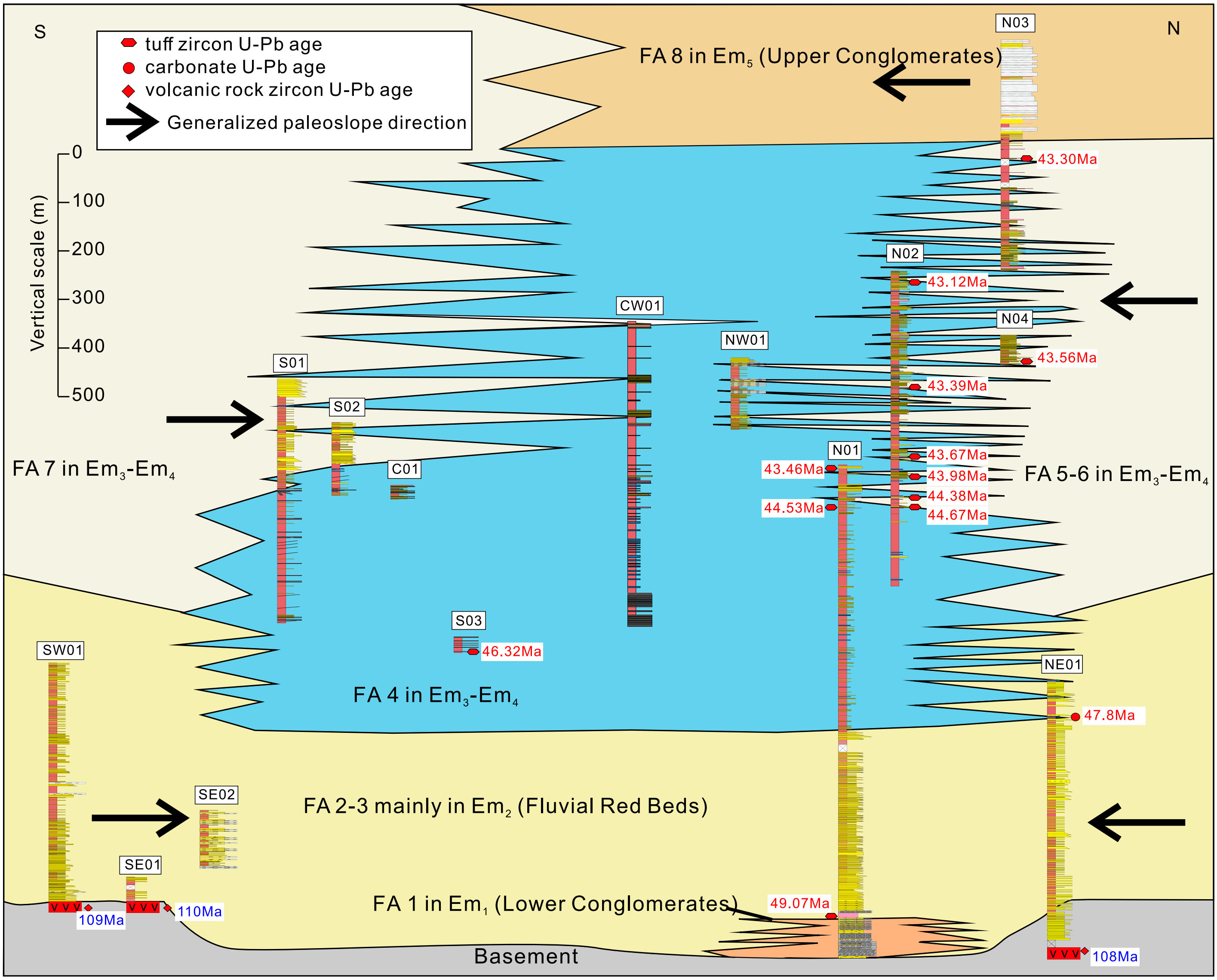

Figure 15. Tentative correlation diagram for measured sections in the Maerguo Formation. The locations of sections can be found in Figure 2A. Correlations were established based on marker beds and tuff geochronology. Generalized paleoslope directions are plotted based on paleocurrent measurements. FA—facies association.

where the Maerguo Formation rests unconformably upon Cretaceous volcanic and Jurassic sedimentary rocks and dips gently to the north.

One interpretation is that the Xianqian Basin was a foreland basin, and the subsidence was controlled by the southward propagation of a thrust belt. This interpretation is consistent with the acceleration of subsidence over time, followed by basin inversion, which could be interpreted to be the transition from forebulge to foredeep and finally to wedge top, related to southward propagation of a thrust load (DeCelles and Giles, 1996). At the same time, the Xianqian Basin is notably unlike other thrust-bounded basins in Tibet, which are elongate and narrow (<15 km in width) in map view, and dominated by kilometers-thick sections of upward-coarsening conglomeratic sequences associated with basin-scale growth strata and overturned synclines (Horton et al., 2002; Kapp et al., 2007; DeCelles et al., 2007; Li et al., 2018). The widespread deposition of the basal fluvial unit around the beginning of deposition in the Xianqian Basin (over >40 km of the basin from north to south, before restoration of any Eocene and younger shortening) suggests a broad area of subsidence that potentially requires another tectonic driver. One possibility is dynamic subsidence due to the localized removal of dense lower lithosphere (e.g., DeCelles et al., 2015; He and Kapp, 2023; McMillan and Schoenbohm, 2023), which would also be consistent with the observed subsidence curve (Fig. 3), stratigraphic patterns, rapid postburial exhumation, and increase in proximal volcanism around the time of maximum basin subsidence (J. He, 2025, personal commun.). We consider this latter possibility in more detail in a companion paper addressing the structural geology of the basin (J. He, 2025, personal commun.).

Based on stratigraphy, sedimentology, provenance, and section correlation, the paleogeographic evolution of the Xianqian Basin can be divided into four stages (Fig. 16). During the first stage between 49.6 Ma and 47.0 Ma,

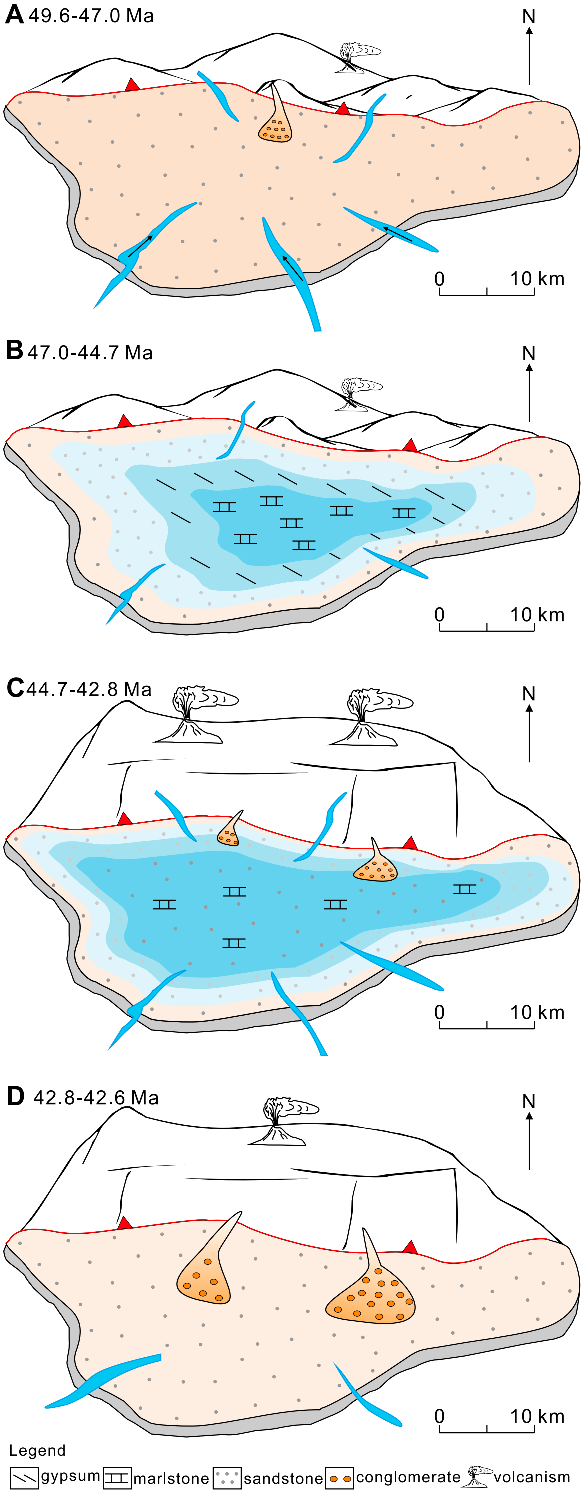

Figure 16. Paleogeography and paleoenvironment of the Xianqian Basin at four periods from ca. 50 Ma to 43 Ma. See text for discussion.

units Em$_1$ and Em$_2$ were deposited. An alluvial-fan environment was developed locally in the northern Xianqian Basin, while fluvial systems dominated along both the northern and southern margins, with bidirectional paleodrainage feeding the basin (Fig. 16A). During the second stage from 47.0 Ma to 44.7 Ma, a lake expanded, resulting in the deposition of limestone, gypsum, and mudrock (Fig. 16B). During the third stage between 44.7 Ma and 42.8 Ma, the lake deepened, and sediments sourced from the Jurassic granitoids and metamorphic rocks to the north of the Xianqian Basin were deposited in deltaic settings along the northern margin. This provenance shift was accompanied by a threefold increase in sediment accumulation rate from 18.0 cm/k.y. to 71.9 cm/k.y. and enhanced tectonic subsidence rate (from ~0.1 mm/yr to ~0.7 mm/yr; Fig. 3). Magmatic activity also intensified during the deposition of unit Em$_4$. The magmatism is interpreted as proximal, as the tuff breccias include abundant granitoid and metamorphic clasts that were likely sourced from local areas to the north of the Xianqian Basin. However, magmatic rocks of 50–43 Ma age have not been reported around the basin, possibly due to complete erosion or insufficient geologic exploration. The southern margin of the Xianqian Basin recorded rejuvenated sand sediment flux, but no significant change in provenance (Fig. 16C), as recorded in unit Em$_4$. During the fourth stage, from 42.8 Ma to 42.6 Ma, the basin was filled quickly, with coarse-grained detritus deposited in an alluvial-fan environment in the northern basin (Fig. 16D). The paleoenvironment in other parts of the basin is unknown because the uppermost unit of the formation is not exposed elsewhere.

5.3. Implications for Paleoenvironments and Tibet Uplift

Deposition of abundant lacustrine gypsum and limestone in unit Em$_3$, along with inward paleoflow directions, suggests that the Xianqian Basin was an internally drained saline lake basin. The disappearance of gypsum, coupled with the presence of punctuated dark-green to gray mudrock and sandstone with leaf and insect fossils in unit Em$_4$ (see Results section; Figs. 11C and 11D), likely indicates a transition to a less arid environment.

Compared to the short-lived Xianqian Basin during 50–43 Ma, the Bangong-Nujiang suture basins were longer-lived (Fig. 17). In the Gerze Basin, the Kangtuo Formation was deposited during ca. 55–40 Ma and dominated by red conglomerates and sandstones, likely also indicating a relatively arid environment (Song et al., 2023). In the Nima-Lunpola-Bangoin basins to the east, coarse deposits of the lower Niubao Formation were deposited earlier than 50 Ma and as young as 40 Ma (Xiong et al., 2022), and the mudrocks in the Bangoin Basin contain abundant biota suggesting subtropical wet environments at ca. 47 Ma (Su et al., 2020). Clumped isotopes of paleosol carbonate in Lunpola (Xiong et al., 2022) and leaf morphotypes in Bangoin (Su et al., 2020) both suggest <2 km paleoelevation.

The Gerze Basin to the south of the Xianqian Basin was suggested to be near sea level around the late Eocene (ca. 36 Ma) based on the presence of marine foraminifera in fine-grained lacustrine strata of the Suonahu Formation (Wei

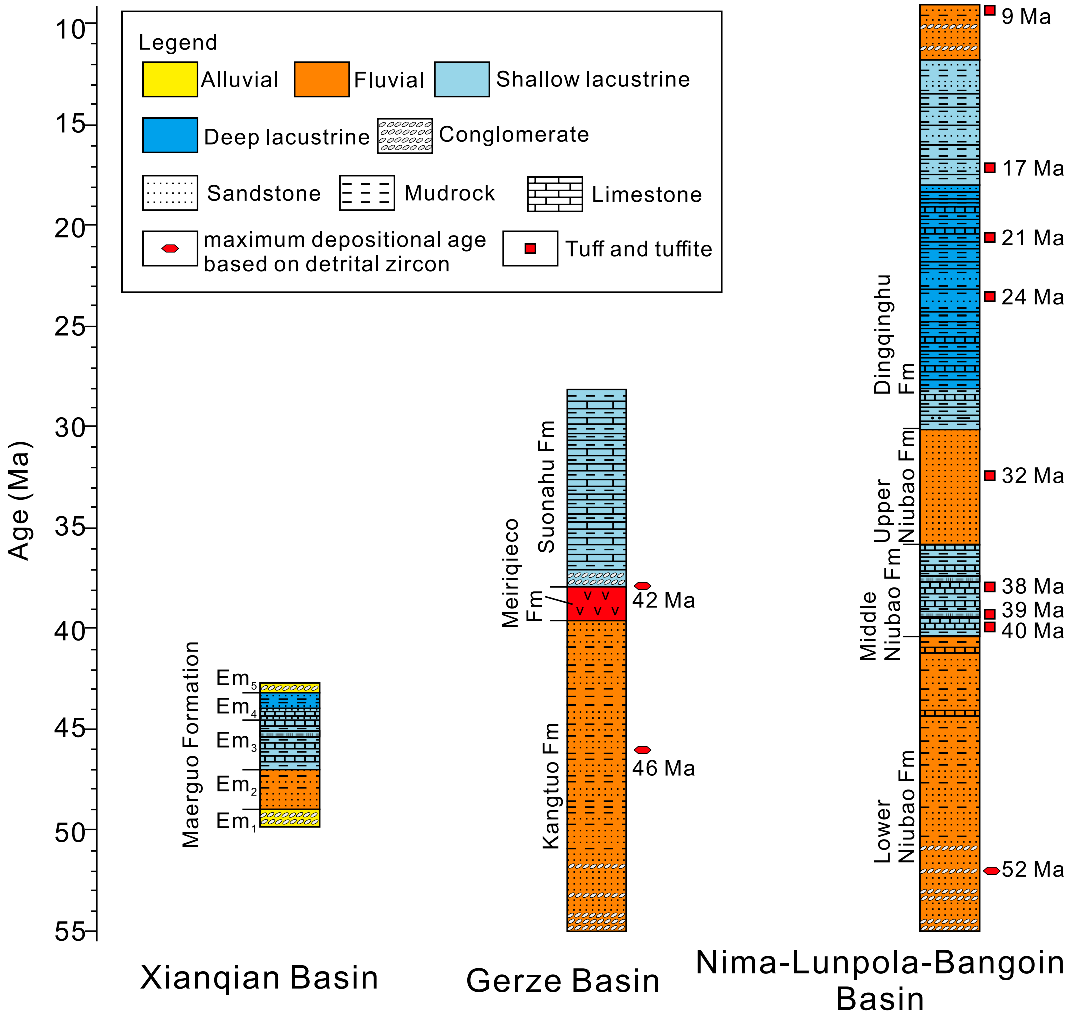

Figure 17. Stratigraphy of the Xianqian Basin in comparison with Gerze (Wei et al., 2016; Song et al., 2023) and Nima-Lunpola Basins (Han et al., 2019; Fang et al., 2020; Xiong et al., 2022).

et al., 2016). The relatively positive δ^{18}O values (−6‰ to −4‰ relative to Vienna Peedee belemnite [VPDB]) of the lacustrine carbonate were interpreted to indicate low paleoelevations close to sea level (Wei et al., 2016) or high paleoelevations due to evaporation (Ingalls et al., 2020). However, recent clumped and oxygen isotopic datasets indicate the existence of shallow burial dolomitization and late-stage telogenetic carbonate precipitation after exhumation to near Earth's surface, which complicates paleoelevation interpretation (Li et al., 2024a). From a geologic perspective, the Gerze Basin should have been lower in paleoelevation than the sediment source area to its north during ca. 55–30 Ma, when the Kangtuo and Suonahu Formations were deposited (Song et al., 2023). In addition, as the Xianqian Basin was deposited on rocks in the hanging wall of the Shiquanhe-Gerze-Amdo thrust system, which was active as early as Early Cretaceous time (Kapp et al., 2005; Li et al., 2022a), its paleoelevation may have been higher than the contemporaneous Gerze Basin, which was deposited in the footwall.

Based on regional basin evolution, we present schematic north-south cross sections to show the four-stage topographic history of central Tibet (Fig. 18). During the first stage, from 49.6 Ma to 47.0 Ma, the Xianqian Basin started to subside (~0.1 mm/yr), and the north-dipping Xianqian thrust in the north activated, possibly associated with growth of a dense lithospheric instability beneath the basin (Fig. 18A) in conjunction with north-south–directed crustal shortening. Scattered magmatism occurred in the Qiangtang interior (Fig. 1B). The Gerze Basin along the Bangong-Nujiang suture zone, developing in the footwall of the Shiquanhe-Gerze-Amdo thrust, was lower in elevation than the Xianqian Basin in the hanging wall (Fig. 18A). Farther south, the southern Lhasa terrane had already risen to >4 km while the Indian lithosphere was subducting northward beneath it (Ding et al., 2014; Ingalls et al., 2018; Ibarra et al., 2023). Then from 47.0 Ma to 44.7 Ma, the Xianqian Basin deepened slightly to form a shallow lake environment. Scattered tuff beds indicate continued but volumetrically minor volcanic activity in the Qiangtang interior (Fig. 18B). During these two stages, the basin subsided at a relatively low rate (Fig. 3), which would be consistent with the slow subsidence expected at the early stages of basin formation associated with lithospheric drips, as also observed in the Arizaro Basin in the Puna Plateau (DeCelles et al., 2015).

From 44.7 Ma to 42.8 Ma, the Xianqian Basin further deepened and was filled with delta-front to prodelta gravity-flow deposits. The basin experienced an acceleration in tectonic subsidence rate from ~0.1 mm/yr to ~0.7 mm/yr at 43.7 Ma, before decelerating to <0.2 mm/yr at ca. 43.3 Ma. The basin subsidence acceleration would be consistent with the acceleration in strain rate as the dense lithosphere root began to sink (He and Kapp, 2023). The increasingly rapid growth and descent of the lithosphere root would cause

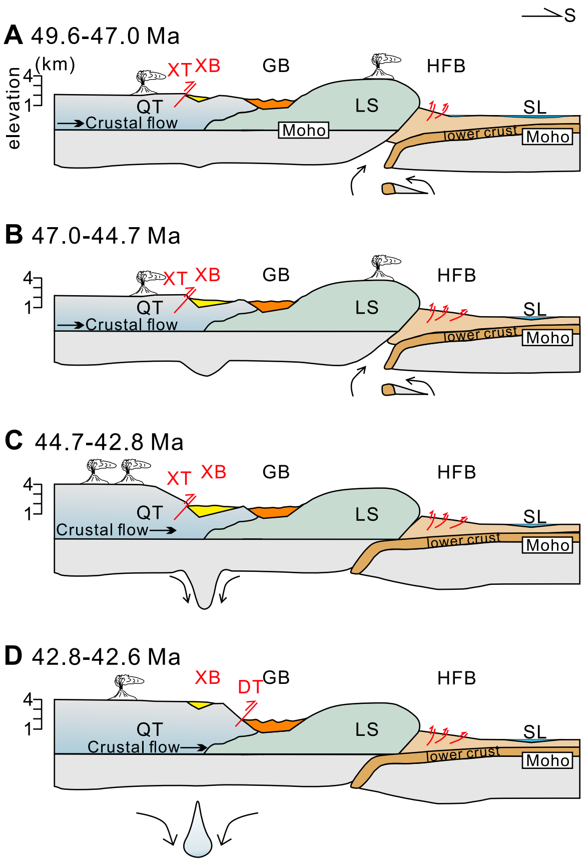

Figure 18. Schematic north-south cross sections show basin evolution during four different stages in the Eocene, which is proposed to have been controlled at least in part by southward propagation of thrust belts in southern Qiangtang and possibly dripping of dense lower lithosphere, as discussed in the text. The sea retreat history and evolution of the Himalaya foreland basin system are after Zhang et al. (2025). LS—Lhasa terrane; QT—Qiangtang terrane; XT—Xianqian thrust; DT—Dongco thrust; XB—Xianqian Basin; GB—Gerze Basin; HFB—Himalaya foreland basin; SL—sea level.

upwelling of asthenosphere and cause partial melting (Wang and Currie, 2015). Volcanism may have occurred in areas proximal to the Xianqian Basin, and this was preserved in the basin as tuff beds. The inferred magmatic heating and addition, coupled with isostatic uplift from crustal thickening due to thrusting (e.g., the Xianqian thrust) and possibly crustal flow, may have elevated the Qiangtang plateau north of the Xianqian Basin from ∼2 km to >4 km (Fig. 18C; A. Ma, 2025, personal commun.).

Tectonic subsidence remained low (<0.2 mm/yr) from 43.3 Ma to 42.6 Ma, but during 42.8–42.6 Ma, the Xianqian Basin was rapidly infilled by alluvial-fan deposits. If the basin formed as a result of lithospheric drip, detachment of the drip would have led to dynamic rebound and isostatic uplift, which could have inverted the basin and resulted in proximal coarse deposition in unit Em$_5$. The Dongco thrust, a segment of the Shiquanhe-Gerze-Amdo thrust system that bounds the north of the Gerze Basin, could also have reactivated and further elevated the Xianqian Basin (Fig. 18D). Alternatively, middle- to lower-crustal flow from the Qiangtang interior may have contributed to crustal thickening beneath the Xianqian Basin and then the Bangong-Nujiang suture basins, which likely played a key role in surface flattening (Li et al., 2024b). However, this latter possibility would be at odds with the interpretation that lithospheric dripping drove surface subsidence, which requires strong coupling between the mantle lithosphere and the upper crust (McMillan and Schoenbohm, 2023).

6. CONCLUSIONS

The Xianqian Basin, oval-shaped with an east-west–trending long axis in the southwestern Qiangtang terrane, was filled with the 50–43 Ma Maerguo Formation. From oldest to youngest, the depositional systems of the Maerguo Formation changed from alluvial fan to fluvial, shallow lacustrine, deltaic and deep lacustrine, and finally to alluvial fan again. Most of the Maerguo Formation clastic sediments were derived from older sedimentary and volcanic rocks surrounding the basin, as suggested by bidirectional paleoflow throughout much of the basin history. A significant shift in sediment sources, from sedimentary and volcanic rocks in a wider drainage to granitoid and metamorphic rocks in a more localized drainage, occurred at ca. 45 Ma in the northern Xianqian Basin. Both the granitoid and metamorphic rocks were sourced from the north of the Xianqian Basin. The presence of abundant continental red beds and gypsum in the lower part of the Maerguo Formation indicates an arid environment. The appearance of plant fragments, insects, bioturbation, dark-colored fine-grained clastic rocks, and other aquatic fossils in the upper part of the Maerguo Formation at ca. 43 Ma suggests less arid climatic conditions.

The Xianqian Basin developed contemporaneously with north-south crustal shortening associated with the Xianqian thrust, as evidenced by syncontractional growth strata in the northern Xianqian Basin. Since basin subsidence occurred simultaneously along both the northern and southern margins of the Xianqian Basin, as evidenced by widespread fluvial deposits of unit Em$_2$, we propose that lithospheric dripping was responsible for the local shortening and basin subsidence. In comparison with the Bangong-Nujiang suture basins, the paleogeographic reconstruction indicates a southward uplift pattern in the Qiangtang plateau. These lines of evidence argue for a Tibetan Plateau that was uplifted not solely in a south-to-north sequence, but also expanded southward, starting from the interior of the Qiangtang terrane.

ACKNOWLEDGMENTS

We thank Yue Guan, Lanlan Tian, and Huan Hu for their assistance with zircon U-Pb dating, Youzhe Jibu for support during the field trip, Gongle Shi and Tao Su for plant fossil identification, Diyin Huang for insect identification, and Tingting Yu for gastropod identification. We are grateful to Science Editor Mihai Ducea and Associate Editor Fangyang Hu for efficient handling. The paper benefited from reviews by Majie Fan, Jiaopeng Sun, Guohui Chen, and an anonymous reviewer. This study was supported by the National Natural Science Foundation of China (grants 42488201 and 42050102), an International Association of Sedimentologists postgraduate research grant, and U.S. National Science Foundation grant EAR-2048656.

REFERENCES CITED

Allen, P.A., and Allen, J.R., 2005, Basin Analysis: Principles and Applications (2nd ed.): Oxford, UK, Blackwell, 560 p.

Baas, J.H., Best, J.L., and Peakall, J., 2011, Depositional processes, bedform development and hybrid bed formation in rapidly decelerated cohesive (mud-sand) sediment flows: Sedimentology, v. 58, no. 7, p. 1953–1987, https://doi.org/10.1111/j.1365-3091.2011.01247.x.

Bohacs, K.M., Carroll, A.R., and Neal, J.E., 2003, Lessons from large lake systems—Thresholds, nonlinearity, and strange attractors, *in* Chan, M.A., and Archer, A.W., eds., Extreme Depositional Environments: Mega End Members in Geologic Time: Geological Society of America Special Paper 370, p. 75–90, https://doi.org/10.1130/0-8137-2370-1.75.

Cant, D.J., and Walker, R.G., 1978, Fluvial processes and facies sequences in the sandy braided South Saskatchewan River, Canada: Sedimentology, v. 25, no. 5, p. 625–648, https://doi.org/10.1111/j.1365-3091.1978.tb00323.x.

Chapman, J.B., and Kapp, P., 2017, Tibetan magmatism database: Geochemistry, Geophysics, Geosystems, v. 18, no. 11, p. 4229–4234, https://doi.org/10.1002/2017GC007217.

DeCelles, P.G., and Giles, K.A., 1996, Foreland basin systems: Basin Research, v. 8, no. 2, p. 105–123, https://doi.org/10.1046/j.1365-2117.1996.01491.x.

DeCelles, P.G., Langford, R.P., and Schwartz, R.K., 1983, Two new methods of paleocurrent determination from trough cross-stratification: Journal of Sedimentary Research, v. 53, no. 2, p. 629–642, https://doi.org/10.1306/212F824C-2B24-11D7-8648000102C1865D.

DeCelles, P.G., Kapp, P., Ding, L., and Gehrels, G.E., 2007, Late Cretaceous to middle Tertiary basin evolution in the central Tibetan Plateau: Changing environments in response to tectonic partitioning, aridification, and regional elevation gain: Geological Society of America Bulletin, v. 119, p. 654–680, https://doi.org/10.1130/B26074.1.

DeCelles, P.G., Kapp, P., Quade, J., and Gehrels, G., 2011, Oligocene–Miocene Kailas basin, southwestern Tibet: Record of postcollisional upper-plate extension in the Indus-Yarlung suture zone: Geological Society of America Bulletin, v. 123, p. 1337–1362, https://doi.org/10.1130/B30258.1.

DeCelles, P.G., Carrapa, B., Horton, B., McNabb, J., Gehrels, G., Boyd, J., Ducea, M., and Kapp, P., 2015, The Miocene Arizaro Basin, central Andean hinterland: Response to partial lithosphere removal, *in* DeCelles, P.G., Ducea, M.N., Carrapa, B., and Kapp, P.A., eds., Geodynamics of a Cordilleran Orogenic System: The Central Andes of Argentina and Northern Chile: Geological Society of America Memoir 212, p. 359–386, https://doi.org/10.1130/2015.1212(18).

Dewey, J.F., Shackleton, R.M., Chang, C., and Sun, Y., 1988, The tectonic evolution of the Tibetan Plateau: Philosophical Transactions of the Royal Society of London A: Mathematical, Physical and Engineering Sciences, v. 327, no. 1594, p. 379–413, https://doi.org/10.1098/rsta.1988.0135.

Dickinson, W.R., 1985, Interpreting provenance relations from detrital modes of sandstones, *in* Zuffa, G.G., ed., Provenance of Arenites: Dordrecht, Netherlands, Springer, North Atlantic Treaty Organization (NATO) Advanced Study Institute (ASI) Series, v. 148, p. 333–361, https://doi.org/10.1007/978-94-017-2809-6_15.

Ding, L., Xu, Q., Yue, Y., Wang, H., Cai, F., and Li, S., 2014, The Andean-type Gangdese Mountains: Paleoelevation record from the Paleocene–Eocene Linzhou Basin: Earth and Planetary Science Letters, v. 392, p. 250–264, https://doi.org/10.1016/j.epsl.2014.01.045.

Ding, L., Kapp, P., Cai, F., Garzione, C.N., Xiong, Z., Wang, H., and Wang, C., 2022, Timing and mechanisms of Tibetan Plateau uplift: Nature Reviews Earth & Environment, v. 3, no. 10, p. 652–667, https://doi.org/10.1038/s43017-022-00318-4.

Dodd, T.J., McCarthy, D.J., Amy, L., Plenderleith, G.E., and Clarke, S.M., 2022, Hybrid event bed character and distribution in the context of ancient deep-lacustrine fan models: Sedimentology, v. 69, no. 4, p. 1891–1926, https://doi.org/10.1111/sed.12979.

Fang, X., Dupont-Nivet, G., Wang, C., Song, C., Meng, Q., Zhang, W., Nie, J., Zhang, T., Mao, Z., and Chen, Y., 2020, Revised chronology of central Tibet uplift (Lunpola Basin): Science Advances, v. 6, no. 50, https://doi.org/10.1126/sciadv.aba7298.

Gabriel, K.R., 1971, The biplot graphic display of matrices with application to principal component analysis: Biometrika, v. 58, no. 3, p. 453–467, https://doi.org/10.1093/biomet/58.3.453.

Garzanti, E., 2017, The maturity myth in sedimentology and provenance analysis: Journal of Sedimentary Research, v. 87, no. 4, p. 353–365, https://doi.org/10.2110/jsr.2017.17.

Garzanti, E., 2019, Petrographic classification of sand and sandstone: Earth-Science Reviews, v. 192, p. 545–563, https://doi.org/10.1016/j.earscirev.2018.12.014.

Garzanti, E., and Andò, S., 2019, Heavy minerals for junior woodchucks: Minerals (Basel), v. 9, p. 148, https://doi.org/10.3390/min9030148.

Garzanti, E., Doglioni, C., Vezzoli, G., and Ando, S., 2007, Orogenic belts and orogenic sediment provenance: The Journal of Geology, v. 115, no. 3, p. 315–334, https://doi.org/10.1086/512755.

Gazzi, P., 1966, Le arenarie del flysch sopracretaceo dell'Appennino modenese: Correlazioni con il flysch di Monghidoro: Mineralogica et Petrographica Acta, v. 12, p. 69–97.

Gibling, M.R., 2006, Width and thickness of fluvial channel bodies and valley fills in the geological record: A literature compilation and classification: Journal of Sedimentary Research, v. 76, no. 5, p. 731–770, https://doi.org/10.2110/jsr.2006.060.

Han, Z., Sinclair, H.D., Li, Y., Wang, C., Tao, Z., Qian, X., Ning, Z., Zhang, J., Wen, Y., and Lin, J., 2019, Internal drainage has sustained low-relief Tibetan landscapes since the early Miocene: Geophysical Research Letters, v. 46, no. 15, p. 8741–8752, https://doi.org/10.1029/2019GL083019.

Haughton, P., Davis, C., McCaffrey, W., and Barker, S., 2009, Hybrid sediment gravity flow deposits—Classification, origin and significance: Marine and Petroleum Geology, v. 26, no. 10, p. 1900–1918, https://doi.org/10.1016/j.marpetgeo.2009.02.012.

He, H., Li, Y., Wang, C., Zhou, A., Qian, X., Zhang, J., Du, L., and Bi, W., 2018, Late Cretaceous (ca. 95 Ma) magnesian andesites in the Biluoco area, southern Qiangtang subterrane, central Tibet: Petrogenetic and tectonic implications: Lithos, v. 302–303, p. 389–404, https://doi.org/10.1016/j.lithos.2018.01.013.

He, J.J., and Kapp, P., 2023, Basin record of a Miocene lithosphere drip beneath the Colorado Plateau: Nature Communications, v. 14, 4433, https://doi.org/10.1038/s41467-023-40147-7.

He, Y.-Z., Yi, C.-X., Xiong, X.-G., Yue, L., and Zhu, X., 2006, Discovery of sporo-pollen fossil of Upper Cretaceous Epoch in the Jiacuo District in north Tibet and its implication: Guizhou Geology, v. 23, no. 1, p. 32–35 [in Chinese with English abstract].

Horton, B.K., Yin, A., Spurlin, M.S., Zhou, J., and Wang, J., 2002, Paleocene–Eocene syncontractional sedimentation in narrow, lacustrine-dominated basins of east-central Tibet: Geological Society of America Bulletin, v. 114, p. 771–786, https://doi.org/10.1130/0016-7606(2002)114<0771:PESSIN>2.0.CO;2.

Hu, X.-M., Ma, A.-L., Xue, W.-W., Garzanti, E., Cao, Y., Li, S.-M., Sun, G.-Y., and Lai, W., 2022, Exploring a lost ocean in the Tibetan Plateau: Birth, growth, and demise of the Bangong-Nujiang Ocean: Earth-Science Reviews, v. 229, https://doi.org/10.1016/j.earscirev.2022.104031.

Hubert, J.F., 1962, A zircon-tourmaline-rutile maturity index and the interdependence of the composition of heavy mineral assemblages with the gross composition and texture of sandstones: Journal of Sedimentary Research, v. 32, no. 3, p. 440–450, https://doi.org/10.1306/74D70CE5-2B21-11D7-8648000102C1865D.

Hussain, A., Haughton, P.D., Shannon, P.M., Turner, J.N., Pierce, C.S., Obradors-Latre, A., Barker, S.P., and Martinsen, O.J., 2020, High-resolution X-ray fluorescence profiling of hybrid event beds: Implications for sediment gravity flow behaviour and deposit structure: Sedimentology, v. 67, no. 6, p. 2850–2882, https://doi.org/10.1111/sed.12722.

Ibarra, D.E., Dai, J., Gao, Y., Lang, X., Duan, P., Gao, Z., Chen, J., Methner, K., Sha, L., and Tong, H., 2023, High-elevation Tibetan Plateau before India-Eurasia collision recorded by triple oxygen isotopes: Nature Geoscience, v. 16, p. 810–815, https://doi.org/10.1038/s41561-023-01243-x.

Ingalls, M., Rowley, D., Olack, G., Currie, B., Li, S., Schmidt, J., Tremblay, M., Polissar, P., Shuster, D.L., and Lin, D., 2018, Paleocene to Pliocene low-latitude, high-elevation basins of southern Tibet: Implications for tectonic models of India-Asia collision, Cenozoic climate, and geochemical weathering: Geological Society of America Bulletin, v. 130, p. 307–330, https://doi.org/10.1130/B31723.1.

Ingalls, M., Rowley, D.B., Currie, B.S., and Colman, A.S., 2020, Reconsidering the uplift history and peneplanation of the northern Lhasa terrane, Tibet: American Journal of Science, v. 320, no. 6, p. 479–532, https://doi.org/10.2475/06.2020.01.

Ingersoll, R.V., Bullard, T.F., Ford, R.L., Grimm, J.P., Pickle, J.D., and Sares, S.W., 1984, The effect of grain size on detrital modes: A test of the Gazzi-Dickinson point-counting method: Journal of Sedimentary Research, v. 54, no. 1, p. 103–116, https://doi.org/10.1306/212F83B9-2B24-11D7-8648000102C1865D.

Jackson, S.E., Pearson, N.J., Griffin, W.L., and Belousova, E.A., 2004, The application of laser ablation–inductively coupled plasma–mass spectrometry to in situ U-Pb zircon geochronology: Chemical Geology, v. 211, no. 1–2, p. 47–69, https://doi.org/10.1016/j.chemgeo.2004.06.017.

Kapp, P., and DeCelles, P.G., 2019, Mesozoic–Cenozoic geological evolution of the Himalayan-Tibetan orogen and working tectonic hypotheses: American Journal of Science, v. 319, no. 3, p. 159–254, https://doi.org/10.2475/03.2019.01.

Kapp, P., Yin, A., Harrison, T.M., and Ding, L., 2005, Cretaceous–Tertiary shortening, basin development, and volcanism in central Tibet: Geological Society of America Bulletin, v. 117, p. 865–878, https://doi.org/10.1130/B25595.1.

Kapp, P., DeCelles, P.G., Gehrels, G.E., Heizier, M., and Ding, L., 2007, Geological records of the Lhasa-Qiangtang and Indo-Asian collisions in the Nima area of central Tibet: Geological Society of America Bulletin, v. 119, p. 917–933, https://doi.org/10.1130/B26033.1.

Law, R., and Allen, M.B., 2020, Diachronous Tibetan Plateau landscape evolution derived from lava field geomorphology: Geology, v. 48, p. 263–267, https://doi.org/10.1130/G47196.1.

Li, C., Zhao, Z., Lu, H., and Li, H., 2022a, Late Mesozoic–Cenozoic multistage exhumation of the central Bangong-Nujiang suture, central Tibet: Tectonophysics, v. 827, https://doi.org/10.1016/j.tecto.2022.229268.

Li, L., Garzione, C.N., Pullen, A., Zhang, P., and Li, Y., 2018, Late Cretaceous–Cenozoic basin evolution and topographic growth of the Hoh Xil Basin, central Tibetan Plateau: Geological Society of America Bulletin, v. 130, p. 499–521, https://doi.org/10.1130/B31769.1.

Li, L., Lu, H., Garzione, C., and Fan, M., 2022b, Cenozoic paleoelevation history of the Lunpola Basin in central Tibet: New evidence from volcanic glass hydrogen isotopes and a critical review: Earth-Science Reviews, v. 231, https://doi.org/10.1016/j.earscirev.2022.104068.

Li, L., DeCelles, P., Kapp, P., Garzione, C., Quade, J., and Yanay, N., 2024a, Constraining carbonate diagenesis using clumped isotope temperatures and U-Pb dating: A case study and implications for paleoelevation interpretations in western central Tibet: Geochimica et Cosmochimica Acta, v. 374, p. 1–14, https://doi.org/10.1016/j.gca.2024.04.007.

Li, L., Garzione, C.N., Lu, H., and Quade, J., 2024b, Neogene surface uplift of the Lunpola Basin in central Tibet: Implications for uplifting and flattening of orogenic plateaus: Earth and Planetary Science Letters, v. 646, https://doi.org/10.1016/j.epsl.2024.118961.

Li, L., Quade, J., Garzione, C., Defliese, W.F., DeCelles, P., and Kapp, P., 2024c, Reliability of micritic carbonates in recording well-preserved isotopic composition and implications for paleoelevation estimates in central Tibet: Geochimica et Cosmochimica Acta, v. 375, p. 186–200, https://doi.org/10.1016/j.gca.2024.04.009.

Li, S., Ding, L., Guilmette, C., Fu, J.J., Xu, Q., Yue, Y.H., and Pinto, R.H., 2017, The subduction-accretion history of the Bangong-Nujiang Ocean: Constraints from provenance and geochronology of the Mesozoic strata near Gaize, central Tibet: Tectonophysics, v. 702, p. 42–60, https://doi.org/10.1016/j.tecto.2017.02.023.

Li, X., Tang, G., Gong, B., Yang, Y., Hou, K., Hu, Z., Li, Q., Liu, Y., and Li, W., 2013a, Qinghu zircon: A working reference for microbeam analysis of U-Pb age and Hf and O isotopes: Chinese Science Bulletin, v. 58, p. 4647–4654, https://doi.org/10.1007/s11434-013-5932-x.

Li, Y., He, J., Wang, C., Santosh, M., Dai, J., Zhang, Y., Wei, Y., and Wang, J., 2013b, Late Cretaceous K-rich magmatism in central Tibet: Evidence for early elevation of the Tibetan Plateau?: Lithos, v. 160–161, p. 1–13, https://doi.org/10.1016/j.lithos.2012.11.019.

Liu, Y., Gao, S., Hu, Z., Gao, C., Zong, K., and Wang, D., 2010, Continental and oceanic crust recycling-induced melt-peridotite interactions in the Trans–North China orogen: U-Pb dating, Hf isotopes and trace elements in zircons from mantle xenoliths: Journal of Petrology, v. 51, no. 1–2, p. 537–571, https://doi.org/10.1093/petrology/egp082.

Ludwig, K., 2008, A Geochronological Toolkit for Microsoft Excel: Berkeley Geochronology Center Special Publication 4, 70 p.

Lyster, S.J., Whittaker, A.C., and Hajek, E.A., 2022, The problem of paleo-planforms: Geology, v. 50, p. 822–826, https://doi.org/10.1130/G49867.1.

Ma, A., Hu, X.-M., Garzanti, E., Han, Z., and Lai, W., 2017, Sedimentary and tectonic evolution of the southern Qiangtang basin: Implications for the Lhasa-Qiangtang collision timing: Journal of Geophysical Research: Solid Earth, v. 122, no. 7, p. 4790–4813, https://doi.org/10.1002/2017JB014211.

Ma, A., Hu, X., Kapp, P., Han, Z., Lai, W., and BouDagher-Fadel, M., 2018, The disappearance of a Late Jurassic remnant sea in the southern Qiangtang block (Shamuluo Formation, Najiangco area): Implications for the tectonic uplift of central Tibet: Palaeogeography, Palaeoclimatology, Palaeoecology, v. 506, p. 30–47, https://doi.org/10.1016/j.palaeo.2018.06.005.

Ma, A., Hu, X., Garzanti, E., BouDagher-Fadel, M., Xue, W., Han, Z., and Wang, P., 2023a, Paleogeographic and tectonic evolution of Mesozoic Qiangtang basins (Tibet): Tectonophysics, v. 862, https://doi.org/10.1016/j.tecto.2023.229957.

Ma, A., Hu, X., Garzanti, E., Pullen, A., BouDagher-Fadel, M., Ji, X., Wang, J., Lai, W., and Xue, W., 2023b, Mid-Cretaceous exhumation of the central Qiangtang mountain range metamorphic rocks as evidenced by the Abushan continental redbeds: Tectonics, v. 42, no. 3, https://doi.org/10.1029/2022TC007520.

Ma, A., Hu, X., Garzanti, E., Xue, W., Schlagintweit, F., Xu, Y., and Lai, W., 2024, Diachronous Cretaceous closure of the Bangong-Nujiang-Shyok Ocean (westernmost central Tibet): Tectonics, v. 43, no. 12, https://doi.org/10.1029/2024TC008280.

McMillan, M., and Schoenbohm, L.M., 2023, Diverse styles of lithospheric dripping: Synthesizing gravitational instability models, continental tectonics, and geologic observations: Geochemistry, Geophysics, Geosystems, v. 24, no. 2, https://doi.org/10.1029/2022GC010488.

Miall, A.D., 1977, A review of the braided-river depositional environment: Earth-Science Reviews, v. 13, no. 1, p. 1–62, https://doi.org/10.1016/0012-8252(77)90055-1.

Mou, S., Wang, C., Wang, M., Chen, R., Zeng, C., Chen, H., Xiong, X., Lu, D., Yue, L., Yi, C.-X., He, Y.-Z., Zhu, X., Bian, S., Xu, A., and Zhao, W., 2005, Geological Report of the 1:250,000 Regional Geological Survey in Jiacuo Area: Ministry of Natural Resources of the People's Republic of China, scale 1:250,000 [in Chinese].

Ori, G.G., 1982, Braided to meandering channel patterns in humid-region alluvial fan deposits, River Reno, Po Plain (northern Italy): Sedimentary Geology, v. 31, no. 3–4, p. 231–248, https://doi.org/10.1016/0037-0738(82)90059-8.

Paton, C., Hellstrom, J., Paul, B., Woodhead, J., and Hergt, J., 2011, Iolite: Freeware for the visualisation and processing of mass spectrometric data: Journal of Analytical Atomic Spectrometry, v. 26, no. 12, p. 2508–2518, https://doi.org/10.1039/c1ja10172b.

Polissar, P.J., Freeman, K.H., Rowley, D.B., McInerney, F.A., and Currie, B.S., 2009, Paleoaltimetry of the Tibetan Plateau from D/H ratios of lipid biomarkers: Earth and Planetary Science Letters, v. 287, no. 1–2, p. 64–76, https://doi.org/10.1016/j.epsl.2009.07.037.

Pullen, A., and Kapp, P., 2014, Mesozoic tectonic history and lithospheric structure of the Qiangtang terrane: Insights from the Qiangtang metamorphic belt, central Tibet, *in* Nie, J., Horton, B.K., and Hoke, G.D., eds., Toward an Improved Understanding of Uplift Mechanisms and the Elevation History of the Tibetan Plateau: Geological Society of America Special Paper 507, p. 71–87, https://doi.org/10.1130/2014.2507(04).

Quade, J., Leary, R., Dettinger, M., Orme, D., Krupa, A., DeCelles, P., Kano, A., Kato, H., Waldrip, R., and Huang, W., 2020, Resetting southern Tibet: The serious challenge of obtaining primary records of paleoaltimetry: Global and Planetary Change, v. 191, https://doi.org/10.1016/j.gloplacha.2020.103194.

Roberts, N.M., Rasbury, E.T., Parrish, R.R., Smith, C.J., Horstwood, M.S., and Condon, D.J., 2017, A calcite reference material for LA-ICP-MS U-Pb geochronology: Geochemistry, Geophysics, Geosystems, v. 18, no. 7, p. 2807–2814, https://doi.org/10.1002/2016GC006784.

Rohrmann, A., Kapp, P., Carrapa, B., Reiners, P.W., Guynn, J., Ding, L., and Heizler, M., 2012, Thermochronologic evidence for plateau formation in central Tibet by 45 Ma: Geology, v. 40, p. 187–190, https://doi.org/10.1130/G32530.1.

Rowley, D.B., and Currie, B.S., 2006, Palaeo-altimetry of the late Eocene to Miocene Lunpola Basin, central Tibet: Nature, v. 439, no. 7077, p. 677–681, https://doi.org/10.1038/nature04506.

Schlische, R.W., 1992, Structural and stratigraphic development of the Newark extensional basin, eastern North America: Evidence for the growth of the basin and its bounding structures: Geological Society of America Bulletin, v. 104, p. 1246–1263, https://doi.org/10.1130/0016-7606(1992)104<1246:SASDOT>2.3.CO;2.

Shen, L., Wang, J., Fu, X., Wei, H., Zhao, J., Xiao, S., and Song, C., 2023, Sedimentary environments of middle Eocene sediments in the northern Qiangtang Basin, northern Tibetan Plateau: Implications for paleoclimate and paleoelevation: Journal of Asian Earth Sciences, v. 245, https://doi.org/10.1016/j.jseaes.2023.105551.

Sláma, J., Košler, J., Condon, D.J., Crowley, J.L., Gerdes, A., Hanchar, J.M., Horstwood, M.S., Morris, G.A., Nasdala, L., and Norberg, N., 2008, Plešovice zircon—A new natural reference material for U-Pb and Hf isotopic microanalysis: Chemical Geology, v. 249, no. 1–2, p. 1–35, https://doi.org/10.1016/j.chemgeo.2007.11.005.

Song, B., Zhang, K., Wei, Y., Jiang, G., Yang, T., Algeo, T.J., Wang, J., and Han, F., 2023, Paleogene sediment provenance in the Gaize Basin: Implications for early Cenozoic paleogeography of central Tibet: Palaeogeography, Palaeoclimatology, Palaeoecology, v. 632, https://doi.org/10.1016/j.palaeo.2023.111860.

Spicer, R.A., Su, T., Valdes, P.J., Farnsworth, A., Wu, F.-X., Shi, G., Spicer, T.E., and Zhou, Z., 2021, Why 'the uplift of the Tibetan Plateau' is a myth: National Science Review, v. 8, no. 1, https://doi.org/10.1093/nsr/nwaa091.

Stacey, J.T., and Kramers, J., 1975, Approximation of terrestrial lead isotope evolution by a two-stage model: Earth and Planetary Science Letters, v. 26, no. 2, p. 207–221, https://doi.org/10.1016/0012-821X(75)90088-6.

Stevenson, C.J., Peakall, J., Hodgson, D.M., Bell, D., and Privat, A., 2020, TB or not TB: Banding in turbidite sandstones: Journal of Sedimentary Research, v. 90, no. 8, p. 821–842, https://doi.org/10.2110/jsr.2020.43.

Strong, E.E., Gargominy, O., Ponder, W.F., and Bouchet, P., 2008, Global diversity of gastropods (Gastropoda; Mollusca) in freshwater: Freshwater animal diversity assessment: Hydrobiologia, v. 595, p. 149–166, https://doi.org/10.1007/s10750-007-9012-6.

Su, T., Farnsworth, A., Spicer, R.A., Huang, J., Wu, F.-X., Liu, J., Li, S.-F., Xing, Y.-W., Huang, Y.-J., and Deng, W.-Y.-D., 2019, No high Tibetan Plateau until the Neogene: Science Advances, v. 5, no. 3, https://doi.org/10.1126/sciadv.aav2189.

Su, T., Spicer, R.A., Wu, F.-X., Farnsworth, A., Huang, J., Del Rio, C., Deng, T., Ding, L., Deng, W.-Y.-D., and Huang, Y.-J., 2020, A middle Eocene lowland humid subtropical "Shangri-La" ecosystem in central Tibet: Proceedings of the National Academy of Sciences of the United States of America, v. 117, no. 52, p. 32,989–32,995, https://doi.org/10.1073/pnas.2012647117.

Vermeesch, P., 2012, On the visualisation of detrital age distributions: Chemical Geology, v. 312–313, p. 190–194, https://doi.org/10.1016/j.chemgeo.2012.04.021.

Wang, C., Zhao, X., Liu, Z., Lippert, P.C., Graham, S.A., Coe, R.S., Yi, H., Zhu, L., Liu, S., and Li, Y., 2008a, Constraints on the early uplift history of the Tibetan Plateau: Proceedings of the National Academy of Sciences of the United States of America, v. 105, no. 13, p. 4987–4992, https://doi.org/10.1073/pnas.0703595105.

Wang, H., and Currie, C.A., 2015, Magmatic expressions of continental lithosphere removal: Journal of Geophysical Research: Solid Earth, v. 120, no. 10, p. 7239–7260, https://doi.org/10.1002/2015JB012112.

Wang, J., Zeng, S., Fu, X., Chen, W., Dai, J., and Ren, J., 2019, New evidence for deposition age of the Suonahu Formation in the Qiangtang Basin: Geological Bulletin of China (Dizhi Tongbao), v. 38, no. 7, p. 1256–1258 [in Chinese with English abstract].

Wang, L., Wang, C., Li, Y., Zhu, L., and Wei, Y., 2011, Organic geochemistry of potential source rocks in the Tertiary Dingqinghu Formation, Nima basin, central Tibet: Journal of Petroleum Geology, v. 34, no. 1, p. 67–85, https://doi.org/10.1111/j.1747-5457.2011.00494.x.

Wang, Q., Wyman, D.A., Xu, J., Dong, Y., Vasconcelos, P.M., Pearson, N., Wan, Y., Dong, H., Li, C., and Yu, Y., 2008b, Eocene melting of subducting continental crust and early uplifting of central Tibet: Evidence from central-western Qiangtang high-K calc-alkaline andesites, dacites and rhyolites: Earth and Planetary Science Letters, v. 272, no. 1–2, p. 158–171, https://doi.org/10.1016/j.epsl.2008.04.034.

Wang, Y., Baars, T.F., Storms, J.E., Martinius, A.W., Gingerich, P.D., and Abels, H.A., 2024, Long-eccentricity pacing of alluvial stratigraphic architecture in the Eocene Bighorn Basin, Wyoming, USA: Geology, v. 52, p. 588–593, https://doi.org/10.1130/G52131.1.

Wei, Y., Zhang, K., Garzione, C.N., Xu, Y., Song, B., and Ji, J., 2016, Low palaeoelevation of the northern Lhasa terrane during late Eocene: Fossil foraminifera and stable isotope evidence from the Gerze Basin: Scientific Reports, v. 6, no. 1, https://doi.org/10.1038/srep27508.

Wen, D.-J., Hu, X., Chapman, T., Zeng, G., Ma, A.-L., and Wang, R.-Q., 2023, Late Cretaceous bimodal volcanic rocks in Shuanghu induced by lithospheric delamination beneath the southern Qiangtang, Tibet: Lithos, v. 460–461, https://doi.org/10.1016/j.lithos.2023.107368.

Wiedenbeck, M., Alle, P., Corfu, F., Griffin, W., Meier, M., Oberli, F., von Quadt, A., Roddick, J., and Spiegel, W., 1995, Three natural zircon standards for U-Th-Pb, Lu-Hf, trace element and REE analyses: Geostandards Newsletter, v. 19, no. 1, p. 1–23, https://doi.org/10.1111/j.1751-908X.1995.tb00147.x.

Wilford, D., Sakals, M., Innes, J., and Sidle, R., 2005, Fans with forests: Contemporary hydrogeomorphic processes on fans with forests in west central British Columbia, Canada, *in* Harvey, A.M., Hather, A.E., and Stokes, M., eds., Alluvial Fans: Geomorphology, Sedimentology, Dynamics: Geological Society, London, Special Publication 251, p. 25–40, https://doi.org/10.1144/GSL.SP.2005.251.01.03.

Woodhead, J.D., and Hergt, J.M., 2000, Pb-isotope analyses of USGS reference materials: Geostandards Newsletter, v. 24, no. 1, p. 33–38, https://doi.org/10.1111/j.1751-908X.2000.tb00584.x.

Wu, F., Miao, D., Chang, M.-m., Shi, G., and Wang, N., 2017, Fossil climbing perch and associated plant megafossils indicate a warm and wet central Tibet during the late Oligocene: Scientific Reports, v. 7, no. 1, p. 878, https://doi.org/10.1038/s41598-017-00928-9.

Xia, D.X., and Liu, S.K., 1997, Lithostratigraphy of Xizang (Tibet) Autonomous Region: Beijing, China University of Geosciences Press, 302 p. [in Chinese with English abstract].

Xiong, Z., Liu, X., Ding, L., Farnsworth, A., Spicer, R.A., Xu, Q., Valdes, P., He, S., Zeng, D., and Wang, C., 2022, The rise and demise of the Paleogene central Tibetan Valley: Science Advances, v. 8, no. 6, https://doi.org/10.1126/sciadv.abj0944.

Xu, Q., Ding, L., Zhang, L., Cai, F., Lai, Q., Yang, D., and Liu-Zeng, J., 2013, Paleogene high elevations in the Qiangtang terrane, central Tibetan Plateau: Earth and Planetary Science Letters, v. 362, p. 31–42, https://doi.org/10.1016/j.epsl.2012.11.058.

Xu, W., Liu, F., and Dong, Y., 2020, Cambrian to Triassic geodynamic evolution of central Qiangtang, Tibet: Earth-Science Reviews, v. 201, https://doi.org/10.1016/j.earscirev.2020.103083.

Xu, Z., Zhao, J., and Wu, Z., 1985, On the Tertiary continental basins and their petroleum potential in Qinghai-Xizang (Tibet) Plateau with Lunpola Basin as example: Contribution to the Geology of the Qinghai-Xizang (Tibet) Plateau, v. 17, p. 391–399 [in Chinese with English summary].

Yin, A., and Harrison, T.M., 2000, Geologic evolution of the Himalayan-Tibetan orogen: Annual Review of Earth and Planetary Sciences, v. 28, no. 1, p. 211–280, https://doi.org/10.1146/annurev.earth.28.1.211.

Yue, L., Mou, S., Zeng, C., and Yi, C., 2006, Age of the Kangtog Formation in the Dinggo-Gyaco area, Qiangtang, northern Tibet, China: Geological Bulletin of China (Dizhi Tongbao), v. 25, no. 1–2, p. 229–232 [in Chinese with English abstract].

Zeng, Y., Ducea, M.N., Xu, J., Chen, J., and Dong, Y.-H., 2021, Negligible surface uplift following foundering of thickened central Tibetan lower crust: Geology, v. 49, p. 45–50, https://doi.org/10.1130/G48142.1.

Zhang, L.-L., Zhu, D.-C., Yang, Y.-H., Wang, Q., Xie, J.-C., and Zhao, Z.-D., 2021, U-Pb geochronology of carbonate by laser ablation MC-ICP-MS: Method improvements and geological applications: Atomic Spectroscopy, v. 42, no. 6, p. 335–348, https://doi.org/10.46770/AS.2021.803.

Zhang, L.-L., Zhu, D.-C., Xie, J.-C., Wang, Q., Kamo, S., Rochín-Bañaga, H., and Xiao, Y., 2023, TARIM calcite: A potential reference material for laser ICPMS in situ calcite U-Pb dating: Journal of Analytical Atomic Spectrometry, v. 38, no. 11, p. 2302–2312, https://doi.org/10.1039/D3JA00222E.

Zhang, Q., Shen, L., Fu, X., Wang, J., Zeng, S., Ruebsam, W., Ahmed, M.S., Shen, H., and Mansour, A., 2024, Eocene climate and hydrology of eastern Asia controlled by orbital forcing and Tibetan Plateau uplift: Earth and Planetary Science Letters, v. 646, https://doi.org/10.1016/j.epsl.2024.118981.

Zhang, Q., Zhang, Q., Ding, L., Wang, T., Ma, X., Gao, B., and Yue, Y., 2025, Seawater retreated from the Tethyan Himalaya of south Tibet at ca. 49 Ma, not ca. 34 Ma: Geological Society of America Bulletin, v. 137, p. 1995–2015, https://doi.org/10.1130/B37675.1.

Zhu, D.-C., Li, S.-M., Cawood, P.A., Wang, Q., Zhao, Z.-D., Liu, S.-A., and Wang, L.-Q., 2016, Assembly of the Lhasa and Qiangtang terranes in central Tibet by divergent double subduction: Lithos, v. 245, no. 1, p. 7–17, https://doi.org/10.1016/j.lithos.2015.06.023.

Science Editor: Mihai Ducea
Associate Editor: Fangyang Hu

Manuscript Received 31 March 2025
Revised Manuscript Received 19 August 2025
Manuscript Accepted 24 September 2025